The Astrophysical Journal, 880:70 (25pp), 2019 August 1 https://doi.org/10.3847/1538-4357/ab29f1

Expanding the Sample of Radio Minihalos in Galaxy Clusters

Simona Giacintucci[1], Maxim Markevitch[2], Rossella Cassano[3], Tiziana Venturi[3], Tracy E. Clarke[1], Ruta Kale[4], and Virginia Cuciti[3]
[1] Naval Research Laboratory, 4555 Overlook Avenue SW, Code 7213, Washington, DC 20375, USA; simona.giacintucci@nrl.navy.mil
[2] NASA/Goddard Space Flight Center, Greenbelt, MD 20771, USA
[3] INAF—Istituto di Radioastronomia, via Gobetti 101, I-40129 Bologna, Italy
[4] National Centre for Radio Astrophysics, Tata Institute of Fundamental Research, Pune University, Pune 411007, India
Received 2019 April 30; revised 2019 June 12; accepted 2019 June 12; published 2019 July 26

Abstract

Radio minihalos are diffuse synchrotron sources of unknown origin found in the cool cores of some galaxy clusters. We use GMRT and VLA data to expand the sample of minihalos by reporting three new minihalo detections (A2667, A907, and PSZ1 G139.61+24.20) and confirming minihalos in five clusters (MACS J0159.8–0849, MACS J0329.6–0211, RXC J2129.6+0005, AS 780, and A3444). With these new detections and confirmations, the sample now stands at 23, the largest sample to date. For consistency, we also reanalyze archival VLA 1.4 GHz observations of seven known minihalos. We revisit possible correlations between the nonthermal emission and the thermal properties of their cluster hosts. Consistent with our earlier findings from a smaller sample, we find no strong relation between the minihalo radio luminosity and the total cluster mass. Instead, we find a strong positive correlation between the minihalo radio power and X-ray bolometric luminosity of the cool core ($r < 70$ kpc). This supplements our earlier result that most, if not all, cool cores in massive clusters contain a minihalo. Comparison of radio and *Chandra* X-ray images indicates that the minihalo emission is typically confined by concentric sloshing cold fronts in the cores of most of our clusters, supporting the hypothesis that minihalos arise from electron reacceleration by turbulence caused by core gas sloshing. Taken together, our findings suggest that the origin of minihalos should be closely related to the properties of thermal plasma in cluster cool cores.

Key words: catalogs – galaxies: clusters: general – radio continuum: galaxies – surveys – X-rays: galaxies: clusters

1. Introduction

Galaxy clusters are filled with tenuous, hot X-ray-emitting plasma, which is their dominant baryonic component. Over the cluster lifetime, it is heated by merger-generated shocks and turbulence and cools via X-ray radiation, which occurs especially fast in the dense cluster cores. This plasma is permeated by tangled magnetic fields and relativistic particles, which contribute only a small fraction of the total energy density but can strongly affect the plasma behavior, as well as provide an interesting window into the cluster physics. The ultrarelativistic electrons in the intracluster medium (ICM) cool rapidly via synchrotron and inverse Compton radiation and have to be continuously energized. Thus, their synchrotron radio emission provides insight into the particle acceleration processes in clusters. Disregarding the radio galaxies often found in clusters, the diffuse radio emission that originates in the ICM comes as three broad phenomena, each apparently representing different acceleration mechanisms and energy sources (see, e.g., van Weeren et al. 2019 for a recent review). Peripheral radio relics are believed to be the result of acceleration at ICM shocks, while giant diffuse radio halos, typically found in disturbed clusters and extending over the whole cluster, are probably caused by electron reacceleration by merger-induced turbulence (e.g., Brunetti & Jones 2014).

The third phenomenon, radio minihalos, is confined to cluster cool cores (e.g., Giacintucci et al. 2017, hereafter G17). Minihalos are not directly powered by radio jets from the active galactic nucleus (AGN) harbored in the central cluster galaxy, nor do they originate from diffusion or other transport mechanisms of relativistic electrons from the AGN. The radio-emitting electrons are instead generated in situ either as a by-product of hadronic collisions of cosmic-ray protons with thermal protons in the ICM or reacceleration of seed relativistic electrons by turbulence in the cool core (e.g., Gitti et al. 2002; Pfrommer & Enßlin 2004; Fujita et al. 2007; Keshet & Loeb 2010; Fujita & Ohira 2013; ZuHone et al. 2013, 2015; Zandanel et al. 2014; for a review, see Brunetti & Jones 2014).

The distinction among these types of faint radio sources is not always clear in the radio data because of the finite instrument resolution and interferometric image quality, as well as projection effects and the presence of unrelated sources such as radio galaxies, but also because there is a continuum of source morphologies. A physically motivated definition of a minihalo that we adopt is given in G17: it is an extended source in the cluster center that (1) does not consist of radio lobes or tails or show any morphological connection (such as jets) to the central cluster AGN and (2) has a radius between 50 kpc and $0.2R_{500}$.[5] Smaller sources can plausibly be explained by diffusion from the central AGN (e.g., Section 6.4 in Giacintucci et al. 2014b), and $0.2R_{500}$ is the typical boundary between the cluster core, where nongravitational processes (cooling, AGNs, and stellar feedback) become important, and the outer, simpler cluster region, where density, temperature, and pressure profiles of the ICM are self-similar (e.g., McDonald et al. 2017 and references therein).

Using a complete cluster sample, G17 showed that minihalos are rather exclusive to cool cores and that most massive ($M_{500} > 6 \times 10^{14}$ $M_{\odot}$) clusters with cool cores possess minihalos. The cool cores often exhibit sloshing-driven X-ray

[5] Here R_{500} is the radius within which the cluster mean total density is 500 times the critical density at the cluster redshift.

cold fronts (e.g., Markevitch & Vikhlinin 2007). In sloshing cores with a minihalo, the radio emission is generally found to be cospatial with the gas sloshing region (e.g., Mazzotta & Giacintucci 2008; Hlavacek-Larrondo et al. 2013; Giacintucci et al. 2014a, 2014b; Gendron-Marsolais et al. 2017, this paper), suggesting a causal link between sloshing and minihalos—e.g., sloshing motions may amplify the magnetic fields (Keshet et al. 2010) and generate turbulence in the cool core, which in turn reaccelerates the relativistic electrons in minihalos (ZuHone et al. 2013). Gas turbulent motions that are sufficiently strong for this scenario have been measured by the *Hitomi* X-ray observatory in the cool core of the Perseus cluster (Hitomi Collaboration et al. 2016), which is host to a radio minihalo (Burns et al. 1992; Sijbring 1993; Gendron-Marsolais et al. 2017).

Even though most minihalos have active radio galaxies at their centers, it is unclear whether there is a relation between these AGNs and the surrounding diffuse radio emission. The lack of a morphological connection to the AGN (i.e., jets or lobes) in high-resolution radio images of minihalos, when available, suggests that the AGN does not directly replenish the minihalo with high-energy electrons. These AGNs could still be a source of electrons for the minihalos by providing seed particles (e.g., from aged, disrupted radio lobes) that are reenergized by turbulence (Cassano et al. 2008; ZuHone et al. 2013). Central AGNs are also a strong candidate source of the heating required to compensate for the otherwise catastrophic X-ray radiative cooling of the gas at the cluster centers (see McNamara & Nulsen 2007 for a review). The dissipation of the AGN-driven turbulence is one of the possible mechanisms by which the energy of the AGN outbursts is transferred to the gas (Zhuravleva et al. 2014). Other proposed mechanisms include heating by cosmic rays (e.g., Guo & Oh 2008; Pfrommer 2013; Yang & Reynolds 2016; Ruszkowski et al. 2017), as well as gas sloshing, which can provide a net heat inflow by bringing the outer, higher-entropy gas into the cool core (ZuHone et al. 2010). If the radio minihalos are generated by turbulence and/or hadronic cosmic-ray interactions, then a connection between the nonthermal radio emission and the nongravitational processes in cool cores (cooling and heating) may exist at a fundamental level (e.g., Fujita & Ohira 2013; Bravi et al. 2016; Jacob & Pfrommer 2017). This makes the minihalos a very interesting physical probe.

From an observational point of view, the detection and study of minihalos is complicated by a combination of their extent and low surface brightness and the presence of the often much brighter central radio galaxy. Sensitive, low-resolution radio observations with a good sampling of the interferometric *uv* plane, particularly at short antenna spacings (ideally, full-synthesis single-dish imaging), are crucial to properly image the extended emission. At the same time, high-resolution images are needed to identify the emission associated with the central galaxy (as well as other possible radio galaxies in or projected onto the cluster core) and rule out the possibility of the large-scale diffuse emission being part of the radio galaxy. For most confirmed minihalos, radio images at different angular resolutions are available (e.g., Govoni et al. 2009; Giacintucci et al. 2014b, 2014a). However, the existing images for a number of minihalo candidates do not sufficiently detail the morphology of the central galaxy; thus, it is not possible to establish whether the AGN is connected to the surrounding extended emission.

In this paper, we present Giant Metrewave Radio Telescope (GMRT) images from our high-resolution follow-up of previously known candidate minihalos in MACS J0159.8–0849,MACS J0329.6–0211, and RXC J2129.6+0005 (Giacintucci et al. 2014b, hereafter G14a; Kale et al. 2015; hereafter K15). We present new GMRT and Very Large Array (VLA) images of the minihalos in AS 780 and A3444 (Venturi et al. 2007; K15). Using GMRT data, we also report on the detection of new minihalos in the cool cores of A2667, A907, and PSZ1 G139.61+24.20. The latter is a newly discovered *Planck* cluster, where a recent LOFAR[6] observation at 144 MHz has revealed faint ultrasteep-spectrum radio emission extending beyond the minihalo region (Savini et al. 2018). For consistency with our minihalo studies (G14a; G17; this paper), we also reanalyze archival, multiconfiguration VLA observations at 1.4 GHz of seven clusters in which minihalos were reported in the literature—A1835, Ophiuchus, A2029, RBS 797, RX J1347.5–1145, MS 1455.0+2232, and 2A 0335+096 (Sarazin et al. 1995; Gitti et al. 2006; 2007; Mazzotta & Giacintucci 2008; Venturi et al. 2008; Govoni et al. 2009; Doria et al. 2012). Radio results presented here have been used for the G17 statistical sample study.

Using our larger sample of confirmed minihalos, we investigate correlations between the radio emission and the properties of the cluster hosts derived from *Chandra* X-ray data. Table 1 lists the minihalos used in our statistical analysis. We do not include clusters with a central extended radio source whose classification as a minihalo is still uncertain or unconfirmed (G14a; G17; van Weeren et al. 2019).

The paper is organized as follows. The radio observations are described in Section 2, our new radio images are presented in Sections 3 and 4, the analysis of the *Chandra* archival X-ray data is described in Section 5, and a brief discussion of our results is given in Section 6. The details of our radio analysis of the previously known minihalos are presented in Appendix A.

We adopt a ΛCDM cosmology with $H_0 = 70\,\mathrm{km\,s^{-1}\,Mpc^{-1}}$, $\Omega_m = 0.3$, and $\Omega_\Lambda = 0.7$. All errors are quoted at the 68% confidence level. For the radio spectral index α, we adopt $S_\nu \propto \nu^{-\alpha}$, where S_ν is the flux density at the frequency ν.

2. Radio Observations

In this section, we describe the new GMRT observations at 1.4 and 1.3 GHz of the clusters MACS J0159.8–0849, MACS J0329.6–0211, RXC J2129.6+0005, and AS 780. For RXC J2129.6+0005 and AS 780, we complement these observations with higher-frequency data retrieved from the VLA archive. We also reanalyze the archive observations of AS 780 (GMRT, 610 MHz), A3444 (VLA,1.4 GHz), A907 (GMRT, 610 MHz), and A2667 (GMRT, 610 MHz and 1.15 GHz). Finally, we present new GMRT data at 1.28 GHz and 610 MHz of the *Planck* cluster PSZ1 G139.61+24.20. Details of all of these observations are provided in Table 2.

In Appendix A, we present our reanalysis of archival VLA observations at 1.4 GHz of A1835, Ophiuchus, A2029, RBS 797, RX J1347.5–1145, MS 1455.0+2232, and 2A 0335+096 (Table 8), known to possess a central minihalo at their center. New images and individual notes on these clusters are presented.

All data were reduced using the NRAO[7] Astronomical Image Processing System (AIPS) package. A description of the

[6] Low Frequency Array; van Haarlem et al. (2013).
[7] National Radio Astronomy Observatory.

Table 1
List of Minihalo Clusters

Cluster Name	R.A.$_{J2000}$ (h, m, s)	Decl.$_{J2000}$ (deg, arcmin, arcsec)	z	Scale (kpc arcsec^{-1})
1	2	3	4	5
Clusters Analyzed in This Paper				
MACS J0159.8–0849	01 59 48.0	−08 49 00	0.405	5.413
MACS J0329.6–0211	03 29 40.8	−02 11 54	0.450	5.759
RXC J2129.6+0005	21 29 37.9	+00 05 39	0.235	3.734
AS 780	14 59 29.3	−18 11 13	0.236	3.746
A3444	10 23 54.8	−27 17 09	0.254	3.958
A907	09 58 22.2	−11 03 35	0.153	2.653
A2667	23 51 40.7	−26 05 01	0.230	3.674
PSZ1 G139.61+24.20[a]	06 22 13.9	+74 41 39	0.267	4.102
A1835	14 01 02.3	+02 52 48	0.253	3.944
Ophiuchus	17 12 25.9	−23 22 33	0.028	0.562
A2029	15 10 55.0	+05 43 12	0.077	1.451
RBS 797	09 47 12.9	+76 23 13	0.354	4.894
RX J1347.5–1145	13 47 30.6	−11 45 10	0.451	5.771
MS 1455.0+2232	14 57 15.1	+22 20 34	0.258	4.001
2A 0335+096	03 38 35.3	+09 57 55	0.036	0.722
Clusters with Literature Radio Information				
A478	04 13 20.7	+10 28 35	0.088	1.646
ZwCl 3146	10 23 39.6	+04 11 10	0.290	4.350
RX J1532.9+3021	15 32 54.4	+30 21 11	0.362[b]	5.048
A2204	16 32 45.7	+05 34 43	0.152	2.643
Perseus	03 19 47.2	+41 30 47	0.018	0.366
RXC J1504.1–0248	15 04 07.5	−02 48 16	0.215	3.494
RX J1720.1+2638	17 20 08.9	+26 38 06	0.164	2.814
Phoenix[c]	23 44 42.2	−42 43 08	0.597	6.670

Notes. Column 1: cluster name. Columns 2–4: cluster coordinates and redshift from the NASA/IPAC Extragalactic Database (NED). Column 5: angular to linear scale conversion. The literature radio information is from G14a, except for Perseus (Sijbring 1993), RXC J1504.1–0248 (Giacintucci et al. 2011), RX J1720.1+2638 (Giacintucci et al. 2014a), and Phoenix (van Weeren et al. 2014).
[a] PSZ1 G139.61+24.20: coordinates and redshift are from the *Planck* SZ cluster catalog (Planck Collaboration et al. 2014).
[b] Crawford et al. (1999).
[c] SPT-CL J2344-4243: coordinates and redshift are from McDonald et al. (2015).

Table 2
Details of the Radio Observations

Cluster	Array	Project	Frequency (GHz)	Bandwidth (MHz)	Date	Time (minutes)	FWHM, PA (arcsec × arcsec, deg)	rms (μJy beam^{-1})
1	2	3	4	5	6	7	8	9
MACS J0159.8−0849	GMRT	28_077	1.39	33	2015 Aug 8	240	2.4 × 2.1, 18	35
MACS J0329.6−0211	GMRT	28_077	1.28	33	2015 Aug 7	123	2.7 × 2.1, 61	23
RXC J2129.6+0005	GMRT	28_077	1.30	33	2015 Jul 4	120	2.6 × 2.1, 82	40
	VLA-B	AH788	4.86	50	2002 Jul 7	60	1.3 × 1.2, 10	22
	VLA-A	AE177	8.46	50	1998 Apr 12	18	0.25 × 0.22, −14	22
AS 780	GMRT	07CRA01	0.61	32	2005 Jan 7	50	6.0 × 3.9, 24	65
	GMRT	30_065	1.30	33	2016 Oct 1	76	3.2 × 1.8, 33	83
	VLA-A	AR517	8.46	50	2003 Jul 24	3	0.4 × 0.3, −1	30
A3444	VLA-BnA	AC696	1.44	50	2003 Oct 2	200	8.3 × 4.0, 3	35
	VLA-DnC	AC696	1.44	50	2004 May 30	260	42.5 × 30.2, 58	50
A907	GMRT	15JHC01	0.61	32	2008 Dec 4	150	6.0 × 4.5, −55	45
A2667	GMRT	10CRA01	0.61	16[a]	2006 Aug 27	80	7.3 × 4.3, 2	50
	GMRT	13HBA01	1.15	16	2007 Nov 19, 20	560	3.6 × 2.3, 11	35
PSZ1 G139.61+24.20	GMRT	28_077	0.61	33	2014 Oct 25	286	7.6 × 5.2, 27	35
	GMRT	27_025	0.61	33	2015 Sept 4	280	6.3 × 3.7, 44	70
	GMRT	30_065	1.28	33	2016 Aug 20	310	3.5 × 2.0, 53	15

Note. Column 1: cluster name. Column 2: radio telescope (for the VLA, the array configuration is also reported). Column 3: project identifier. Columns 4–7: observation frequency, bandwidth, date, and total time on source. Column 8: FWHM and position angle of the array, obtained for ROBUST = 0 in IMAGR. Column 9: image rms level (1σ).
[a] The cluster was observed using both the USB and LSB; however, due to residual RFI and other errors affecting the LSB data, we chose to use only the USB data set.

Table 3
Radio Flux Density and Spectral Index

Cluster Name	Source	ν (GHz)	S_ν (mJy)	α	References
1	2	3	4	5	6
MACS J0159.8–0849	S1	1.39	34.0 ± 1.7	−0.57 ± 0.04	1
		1.40	35.0 ± 1.8		2
		8.46	94.8 ± 4.8		2
	MH	1.39	∼2	⋯	1
		1.40	2.4 ± 0.2		2
MACS J0329.6–0211	S1	1.30	3.9 ± 0.2	⋯	1
		1.40	3.8 ± 0.2		2
	MH	1.30	4.5 ± 0.4	⋯	1
		1.40	3.8 ± 0.4		2
RXC J2129.6+0005	S1	0.24	87 ± 5	0.77 ± 0.02	3
		0.61	48.9 ± 2.5		3
		1.30	25.3 ± 1.3		1
		1.40	24 ± 1.2		3
		4.86	8.6 ± 0.3		1
		8.46	5.6 ± 0.2		1
	MH	0.24	21.0 ± 1.6	1.2 ± 0.1	3
		0.61	8.0 ± 0.7		3
		1.30	2.5 ± 0.2		1
		1.40	2.4 ± 0.2		3
AS 780	S1	0.61	102 ± 8	−0.17 ± 0.04	1
		1.30	101 ± 5		1
		8.46	160 ± 8		1
	MH	0.61	34 ± 2	<1.49	1
		1.30	>11		1
A3444	S1	1.44	1.41 ± 0.07	⋯	1
	MH	1.44	12.1 ± 0.9	⋯	1
A907	S1	0.61	117 ± 9	⋯	1
	S2	0.61	42 ± 3	⋯	1
	MH	0.61	34.9 ± 5.6	⋯	1
A2667	S1	0.61	20.1 ± 1.6	0.5 ± 0.1	1
		1.15	14.8 ± 0.7		1
	S2	0.61	3.7 ± 0.3	0.7 ± 0.1	1
		1.15	2.4 ± 0.1		1
	MH	0.61	15.3 ± 1.2	1.0 ± 0.2	1
		1.15	8.3 ± 0.7		1
PSZ1 G139.61+24.20	S1	0.61	1.9 ± 0.2	1.05 ± 0.16	1
		1.28	0.87 ± 0.05		1
	S2	0.61	0.25 ± 0.02	0.14 ± 0.02	1
		1.28	0.18 ± 0.01		1
	MH	0.14	12 ± 1.8	1.33 ± 0.08	4
		0.61	2.3 ± 0.8		1
		1.28	0.65 ± 0.08		1

Note. Column 1: cluster name. Column 2: radio source. Column 3: frequency. Column 4: flux density. Column 5: integrated spectral index, computed between the lowest and highest frequencies reported in the table. Column 6: reference for the radio flux, i.e., (1) this work; (2) G14a; (3) K15; (4) Savini et al. (2018).

GMRT and VLA data reduction is given in Sections 2.1 and 2.2, respectively.

For all clusters, the flux densities of individual radio galaxies and minihalos are summarized in Table 3 (Table 9 for the newly analyzed clusters with previously known minihalos). The position, size, and flux density of the unresolved radio galaxies were determined by fitting the sources with a Gaussian model (JMFIT). For extended radio galaxies, we measured the total flux density by integration within the $+3\sigma$ surface brightness contour. As in G14a, the flux density of minihalos was obtained by measuring the total flux in circular regions of a radius that progressively increased from the radius encompassing the $+3\sigma$ isocontour until the integrated flux density reached saturation. The uncertainty on the minihalo flux density was estimated as described in G14a. For all minihalos, size ($R_{\rm MH}$, measured as in G14a) and luminosity at 1.4 GHz are summarized in Table 4, which also includes eight minihalos with literature information. The table also reports the 1.4 GHz luminosity of the central radio galaxy.

2.1. GMRT Data Reduction

The GMRT data were collected in spectral-line observing mode using the software back end for all clusters (with the exception of A907 and A2667), which provides a total observing bandwidth of 33.3 MHz, subdivided into 256 channels. The observations of A907 at 610 MHz and A2667 at 1.15 GHz were taken with the old hardware correlator using a 256-channel band of 16 MHz width at

Table 4
Properties of Minihalos

Cluster Name	R_{MH} (kpc)	$P_{MH,1.4\ GHz}$ (10^{24} W Hz^{-1})	$P_{BCG,1.4\ GHz}$ (10^{24} W Hz^{-1})	References
1	2	3	4	5
		Clusters Analyzed in This Paper		
MACS J0159.8–0849	90	1.40 ± 0.14	20.3 ± 0.1	2
MACS J0329.6–0211	70	2.84 ± 0.30	2.8 ± 0.1	2
PSZ1 G139.61+24.20	50	0.13 ± 0.02[a]	<0.007[a]	1
A907	65	0.9 ± 0.2[b]	4.1 ± 0.4[b]	1
AS 780	50	>1.7[c]	17 ± 1[c]	1
A3444	120	2.4 ± 0.2	0.28 ± 0.01	1
RX J2129.6+0005	80	0.40 ± 0.03	3.1 ± 0.2	6
A2667	70	1.1 ± 0.1[d]	2.1 ± 0.1[d]	1
A1835	240	1.19 ± 0.25	6.3 ± 0.3	1
Ophiuchus	250	0.11 ± 0.02	0.064 ± 0.003	1
A2029	270	0.28 ± 0.04	7.4 ± 0.4	1
RBS 797	120	2.20 ± 0.24	7.6 ± 0.4	1
RX J1347.5–1145	320	26.7 ± 2.1	22.7 ± 1.1	1
MS 1455.0+2232	120	1.75 ± 0.23	0.96 ± 0.05	1
2A 0335+096	70	0.06 ± 0.01	0.058 ± 0.003	1
		Clusters with Literature Radio Information		
A478	160	0.32 ± 0.06	0.60 ± 0.03	2
ZwCl 3146	90	1.4 ± 0.3	0.8 ± 0.2	2
RX J1532.9+3021	100	3.35 ± 0.17	7.0 ± 0.4	2
A2204	50	0.54 ± 0.05	3.7 ± 0.2	2
Perseus	130	2.18 ± 0.11	13.4 ± 0.1[e]	3
RXC J1504.1–0248	140	2.70 ± 0.14	5.7 ± 0.3	4
RX J1720.1+2638	140	5.33 ± 0.32	0.50 ± 0.02	5
Phoenix	230	9.6 ± 3.1[f]	73.9 ± 7.4[g]	7

Notes. Column 1: cluster name. Column 2: average radius of the minihalo (estimated as in G14a). Column 3: radio luminosity of the minihalo at 1.4 GHz. Column 4: radio luminosity of the BCG at 1.4 GHz. Column 5: references—(1) this work; (2) G14a; (3) Sijbring (1993); (4) Giacintucci et al. (2011); (5) Giacintucci et al. (2014a); (6) K15; (7) van Weeren et al. (2014).
[a] Extrapolated from 1.28 GHz (Section 4.3).
[b] Extrapolated from 610 MHz (Section 4.1).
[c] Extrapolated from 1.30 GHz (Section 3.4).
[d] Extrapolated from 1.15 GHz (Section 4.2).
[e] From NVSS.
[f] Extrapolated from $S_{MH,610\ MHz} = 17 \pm 5$ mJy assuming $\alpha = 1.0 \div 1.3$.
[g] Extrapolated from $S_{BCG,610\ MHz} = 87.9 \pm 9.0$ mJy assuming $\alpha = 0.6 \div 0.8$.

1.15 GHz and two 16 MHz wide upper-side and lower-side (USB and LSB) bands at 610 MHz, each having 128 channels.

We accurately inspected the data and found that all observations were in part impacted by radio frequency interference (RFI). After an initial step of flux and bandpass calibration using standard calibration sources (3C 48, 3C 147, and 3C 286), we used RFLAG to excise RFI-affected visibilities, followed by manual flagging to remove residual bad data. The flux and bandpass calibration was then recomputed and applied to the data. The flux densities of the primary calibrators were set in SETJY using the Perley & Butler (2013) coefficients. Phase calibrators, observed several times during the observation, were used to calibrate the data in phase. A number of phase-only self-calibration cycles and imaging were applied to the target visibilities to correct residual phase errors. To compensate for the non-complanarity of the array, we used wide-field imaging in each step of the self-calibration process to produce the final images, decomposing the primary beam area into ~60–80 smaller facets at 610 MHz and ~30–50 facets at frequencies near 1 GHz. Finally, to improve the dynamic range of the final images, we used PEELR to "peel" problematic nearby bright sources whose sidelobes affected the area of the target. The final images were corrected for the GMRT primary beam response using PBCOR.[8] Residual amplitude errors are estimated to be within 5% at 1 GHz and 8% at 610 MHz (Chandra et al. 2004).

Table 2 provides the restoring beams and rms noise levels (1σ) of the final images, obtained using the "robustness" parameter (Briggs 1995) ROBUST = 0 in IMAGR. For each cluster, we made sets of images with different angular resolution and weighting schemes, ranging from pure uniform weighting (ROBUST = −5) to natural weighting (ROBUST = +5), to enhance the extended emission. The higher-resolution images were used to identify the radio source associated with the brightest cluster galaxy (BCG) and other possible radio galaxies in (or projected onto) the cluster core region. We also produced images by cutting the innermost region of the *uv* plane and using the remaining long baselines ($\gtrsim$1–2 kλ) to better evaluate the contribution of the discrete sources. Low-resolution images were used to map the diffuse radio emission.

[8] http://www.ncra.tifr.res.in:8081/~ngk/primarybeam/beam.html

2.2. VLA Data Reduction

The VLA data were calibrated and reduced following standard procedure. For each cluster, the observations in different array configurations were processed and imaged separately. Several loops of imaging and self-calibration were applied to each data set to reduce the effects of residual phase errors in the images. Tables 2 and 8 summarize the radio beams and 1σ noise levels of the final images, made using a ROBUST = 0. When possible, data from different dates and configurations were combined together in the *uv* or image plane. As for the GMRT data, we used a set of images with different angular resolution, weighting schemes, and *uv* range to identify discrete radio galaxies and map the diffuse minihalos.

The flux density scale was set using standard calibration sources (3C 48, 3C 147, and 3C 286) and the Perley & Butler (2013) coefficients. Residual amplitude errors are within 5%.

3. Minihalo Confirmation

In G14a, we suggested the presence of a minihalo in the clusters MACS J0329.6–0211 and MACS J0159.8–0849, based on VLA 1.4 GHz images at 5″ resolution. In K15, GMRT images at 235 and 610 MHz revealed a central diffuse radio source in RXC J2129.6+0005, which was classified as a minihalo. A possible minihalo was reported at the center of AS 780 and A3444 by Venturi et al. (2007) using GMRT observations at 610 MHz. However, due to the lack of images of all of these clusters with a finer angular resolution, it was not possible to exclude the possibility that the observed extended emission is sustained directly by the central AGN through large-scale jets, rather than being an actual minihalo. Here we present new high-resolution GMRT and VLA images that show no evidence of such jets (or other radio features on the minihalo scale directly connected to the AGN), thus confirming a minihalo in all of these clusters.

3.1. MACS J0159.8–0849

MACS J0159.8–0849 is a relaxed, cool-core cluster at redshift $z = 0.405$ that is host to a candidate minihalo (G14a). Using the GMRT at 1.39 GHz, we imaged the cluster center at 2″ resolution. Our image is shown in Figure 1. As a reference, the first contour of the VLA 1.4 GHz image of the minihalo from G14a is reported in magenta.

The radio source associated with the BCG (S1) is unresolved in our new image at 1.39 GHz. Its flux density is $S_{1.39\,\mathrm{GHz}} = 34.0 \pm 1.7$ mJy (Table 3), which is consistent with 35.0 ± 1.8 mJy measured by the VLA at 1.4 GHz. In the surroundings of the BCG, we detect only hints of the faint diffuse emission seen in the much higher sensitivity VLA image ($1\sigma = 15\ \mu$Jy beam^{-1}). To enhance the extended emission, we made images at slightly lower resolution (down to ∼5″, same as the VLA image) using values of ROBUST > 1 and tapering the *uv* data to weight down the long baselines. However, due to the higher noise in these images ($1\sigma \sim 40\ \mu$Jy beam^{-1}), we were not able to map the diffuse emission around S1. On the other hand, integration over the area enclosed by the VLA isocontour in Figure 1 reveals an excess of ∼2 mJy after subtraction of the flux of S1. Such flux excess is only ∼20% less than the minihalo flux density measured on the VLA image

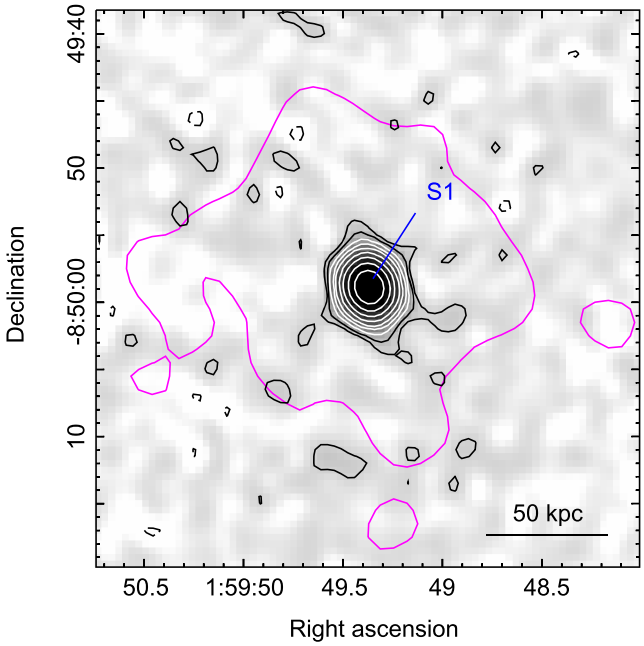

Figure 1. MACS J0159.8–0849 GMRT image at 1.39 GHz (gray scale and black and white contours). The unresolved source S1 is associated with the BCG. The restoring beam is 2.″4 × 2.″1 in PA 18°, and the rms noise level is $1\sigma = 35\ \mu$Jy beam^{-1}. Contours are 0.07, 0.14 (black), 0.28, 0.56, 1, 2, 4, 8, 16, and 32 (white) mJy beam^{-1}. Contours at −0.07 mJy beam^{-1} are shown as dashed. For a comparison, the first contour from the VLA 1.4 GHz image of G14a (their Figure 5) is reported in magenta. The contour level is 0.045 mJy beam^{-1} for a 5″ circular beam.

(2.4 ± 0.2 mJy), thus confirming the presence of an extended component that is not well imaged by our shallow GMRT observation.

Even though higher-sensitivity images are needed to adequately map the minihalo, the absence in Figure 1 of bright jets and/or lobes on the scale of the minihalo suggests that the central radio galaxy and outer extended emission are not morphologically connected. As a further note, the BCG is still unresolved at the subarcsecond resolution of a VLA-A configuration observation at 8.5 GHz (G14a). This indicates that any possible extended lobes/jets associated with S1 must be smaller than ∼2 kpc.

3.2. MACS J0329.6–0211

MACS J0329.6–0211 is a distant ($z = 0.45$) relaxed cluster with a bright, low-entropy cool core (Cavagnolo et al. 2009). Figure 2 presents our new GMRT 1.28 GHz image at a resolution of 2.″7 × 2.″1, overlaid on the optical *Hubble Space Telescope* (*HST*) and X-ray *Chandra* images. The diffuse minihalo, first reported by G14a, is clearly detected in the cluster core region. It has a size of ∼50 kpc in radius, which is comparable to its extent in the G14a VLA 1.4 GHz image at 5″ resolution. No large-scale jets or plumes connect the diffuse emission to the central radio galaxy (S1), which is unresolved, thus limiting its size to less than 15 kpc. Observations at subarcsecond resolution are needed to reveal the details of its radio structure at smaller scales. We measure a flux density of $S_{1.28\,\mathrm{GHz}} = 3.9 \pm 0.2$ mJy for the BCG and $S_{1.28\,\mathrm{GHz}} = 4.5 \pm 0.4$ mJy for the minihalo (Table 3).

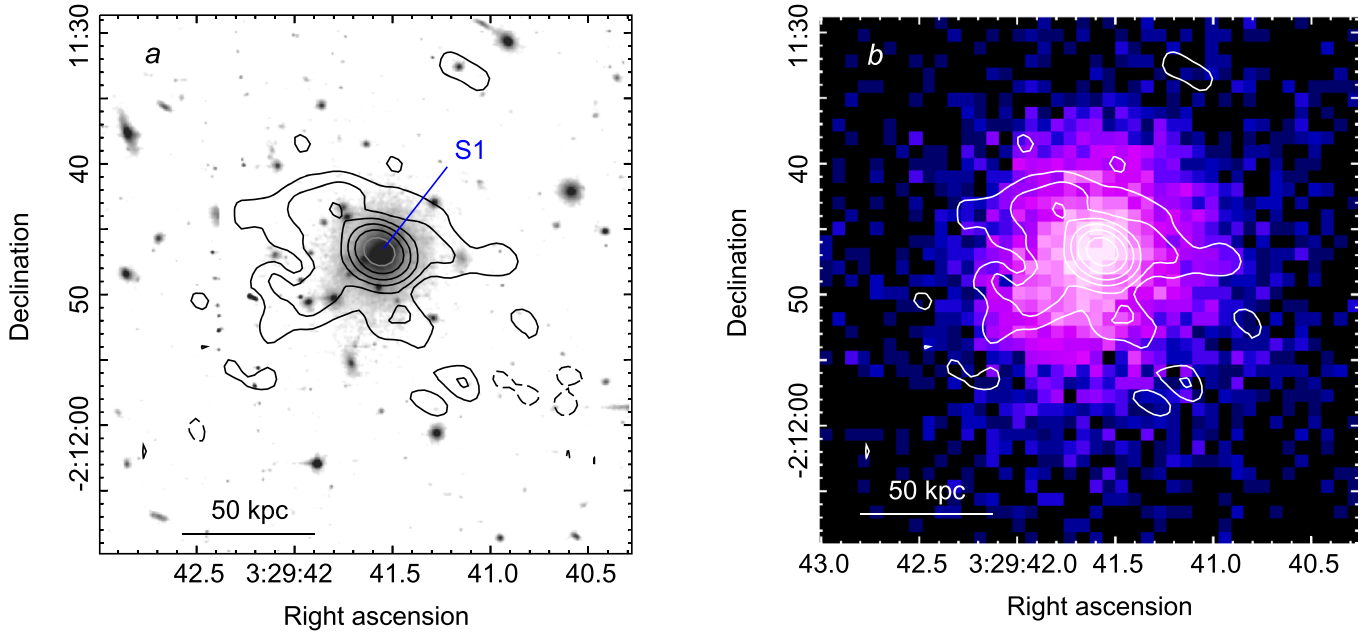

Figure 2. MACS J0329.6–0211. (a) GMRT contours at 1.28 GHz of the central unresolved radio galaxy (S1) and surrounding minihalo, overlaid on an *HST* ACS image (ID: 12452). The radio image has a restoring beam of $2\farcs7 \times 2\farcs1$ in PA 61° and an rms noise level of $1\sigma = 23$ μJy beam^{-1}. Contours are spaced by a factor of 2, starting from $+3\sigma$. Contours at -3σ are shown as dashed. (b) GMRT 1.28 GHz contours, same as panel (a), overlaid on the *Chandra* combined X-ray image in the 0.5–4 keV band.

3.3. RXC J2129.6+0005

At $z = 0.235$, RXC J2129.6+0005 is a relaxed cool-core cluster. A central minihalo was reported by K15, based on a GMRT observation at 610 MHz. In Figure 3(a), we present our new higher-resolution GMRT image at 1.30 GHz. The image detects only the innermost $r \sim 35$ kpc portion of the diffuse source seen at lower frequency (magenta contour). The extended emission encompasses a compact source associated with the BCG (S1). This latter is still pointlike in a 4.86 GHz image at $1''$ resolution, obtained from reanalysis of archival VLA data (Table 2; image not shown here). The source structure is finally unveiled at 8.46 GHz (Figure 3(b)), which resolves the emission into a bright, compact component (possibly the core) coincident with the optical peak in the SDSS[9] image and a fainter ∼4 kpc jet pointing southeast. Hints of a much fainter counterjet are visible on the opposite side of the putative core. A comparison between the radio and X-ray *Chandra* images in Figure 3(c) shows that the diffuse emission detected at 1.30 GHz is centrally located and permeates the brightest part of the cluster core, as seen in other minihalo clusters.

The flux densities of S1 are summarized in Table 3, along with the measurements at lower frequencies by K15. Its spectral index is $\alpha = 0.77 \pm 0.02$ between 235 MHz and 8.46 GHz. For the minihalo, we measure a flux density of $S_{1.30\,\mathrm{GHz}} = 2.5 \pm 0.2$ mJy in the region enclosed by the magenta contour in Figure 3(a). A flux of $S_{1.4\,\mathrm{GHz}} = 2.4 \pm 0.2$ mJy, consistent with our measurement, was estimated by K15 from a comparison between the NVSS[10] and FIRST[11] images. The minihalo has an inferred spectral index of $\alpha = 1.2 \pm 0.1$ between 235 MHz and 1.4 GHz.

[9] Sloan Digital Sky Survey.
[10] NRAO VLA Sky Survey; Condon et al. (1998).
[11] Faint Images of the Radio Sky at Twenty cm; Becker et al. (1995).

3.4. AS 780

At $z = 0.236$, AS 780 is a relaxed cluster with a regular X-ray morphology on large scales. The X-ray surface brightness profile peaks at the BCG, and the gas temperature declines toward the center (e.g., G17), as typically observed in other cool-core clusters. Hints of diffuse radio emission around the central radio galaxy were reported at 610 MHz by Venturi et al. (2007). We have obtained new images at 610 MHz by reanalyzing the Venturi et al. data and compared them to higher-resolution images at 1.30 and 8.46 GHz, as well as to optical (from Pan-STARRS-1[12]) and X-ray (from *Chandra*) images of the cluster central region (Figure 4). The 8.46 GHz image (white contours in panel (b)) shows an extended (∼8 kpc) core-dominated and double-jet radio source, coincident with the dominant optical galaxy and central X-ray point source in the *Chandra* image (panel (d)). The source is embedded in a region of diffuse emission at 1.30 GHz (black contours), which corresponds to the innermost part of the minihalo detected at 610 MHz (panel (a)). The size of the minihalo is ∼50 kpc in radius at 610 MHz. As indicated by a comparison between the radio and X-ray emission (panels (c) and (d)), the minihalo is cospatial with the bright X-ray cool core and edged by a pair of possible cold fronts symmetric with respect to the cluster center.

The flux densities of the central radio galaxy S1 at all frequencies are summarized in Table 3. Its spectrum is inverted with $\alpha = -0.17 \pm 0.04$ between 610 MHz and 8.46 GHz. No high-resolution images at 1.4 GHz (e.g., from FIRST) are available for this source; therefore, we estimate its radio luminosity at 1.4 GHz by extrapolating the 1.3 GHz flux density with $\alpha = -0.17 \pm 0.04$. We obtain $S_{\mathrm{BCG,1.4\,GHz}} = 102.3 \pm 0.3$ and $P_{\mathrm{BCG,1.4\,GHz}} = (17 \pm 1) \times 10^{24}$ W Hz^{-1} (Table 4).

[12] Panoramic Survey Telescope and Rapid Response System; Chambers et al. (2016).

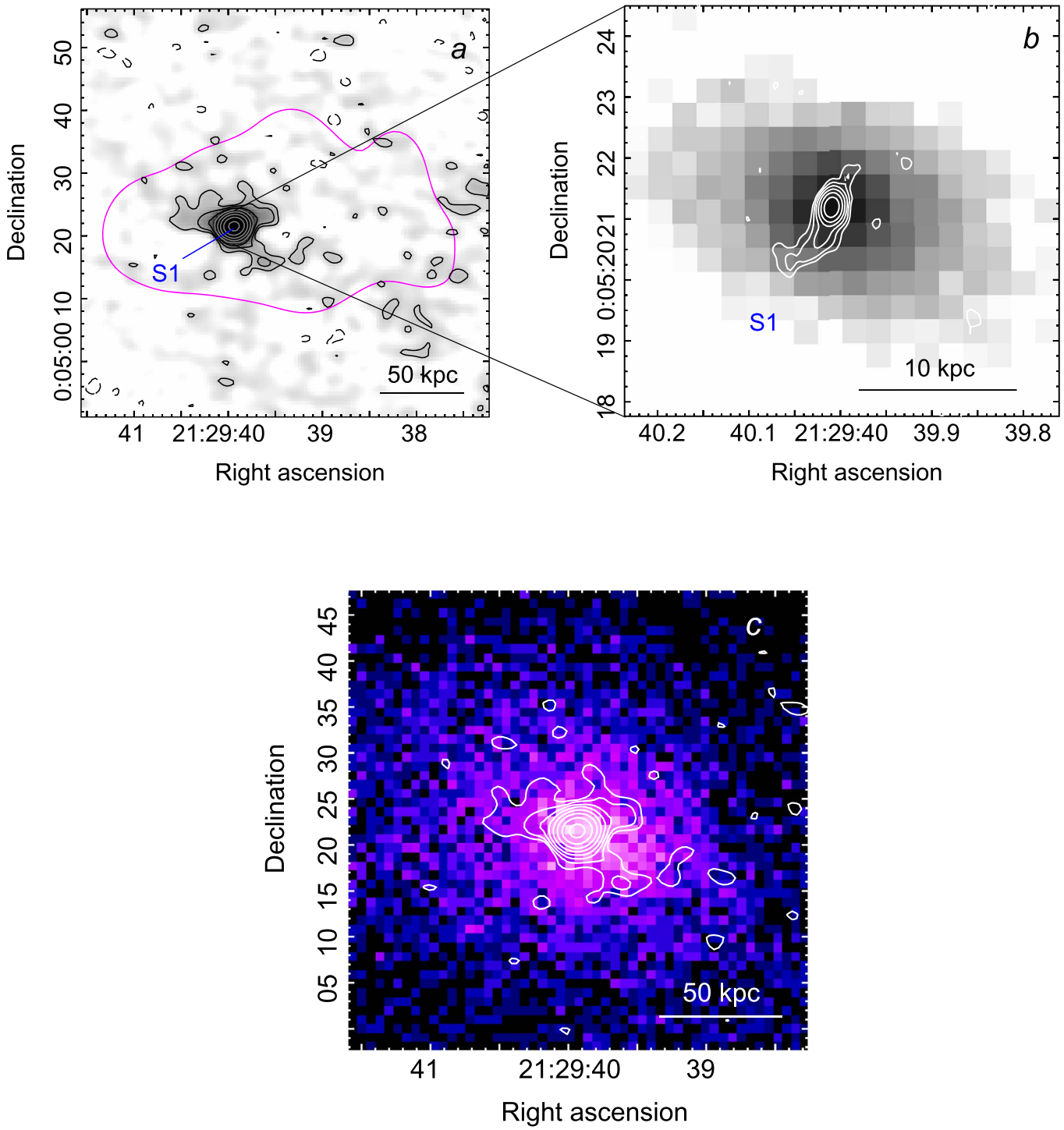

Figure 3. RXC J2129.6+0005. (a) GMRT image at 1.30 GHz (gray scale and black and gray contours) of the central radio galaxy (S1) and innermost part of the minihalo. The restoring beam is $2\farcs6 \times 2\farcs1$ in PA 82°, and the rms noise level is $1\sigma = 45$ μJy beam^{-1}. Contours are spaced by a factor of 2 from 0.12 mJy beam^{-1}. Contours at -0.12 mJy beam^{-1} are shown as dashed. The first contour from the GMRT 610 MHz image of the minihalo from K15 (their Figure 2) is reported in magenta. The contour level is 0.33 mJy beam^{-1} for a $11\farcs6 \times 10\farcs6$ beam. (b) VLA contours at 8.46 GHz of S1, overlaid on the *r*-band SDSS image. The radio image has a restoring beam of $0\farcs33 \times 0\farcs23$ in PA -9°. The rms noise level is $1\sigma = 22$ μJy beam^{-1}. Contours are spaced by a factor of 2 from 0.06 mJy beam^{-1}. (c) GMRT 1.30 GHz contours, same as panel (a), overlaid on the *Chandra* X-ray image in the 0.5–4 keV band.

The minihalo has a flux of $S_{\rm MH,610\,MHz} = 34 \pm 2$ mJy. At 1.30 GHz, where only part of the minihalo is detected, we measure $S_{\rm MH,1.30\,GHz} = 11 \pm 1$ mJy, which has to be considered a lower limit to the actual flux of the minihalo at this frequency. This translates into a spectral index $\alpha < 1.45$ between 610 MHz and 1.30 GHz and an estimated flux density $S_{\rm MH,1.4\,GHz} > 10$ mJy, corresponding to a limit of $P_{\rm MH,1.4\,GHz} > 1.7 \times 10^{24}$ W Hz^{-1} in radio power (Table 4).

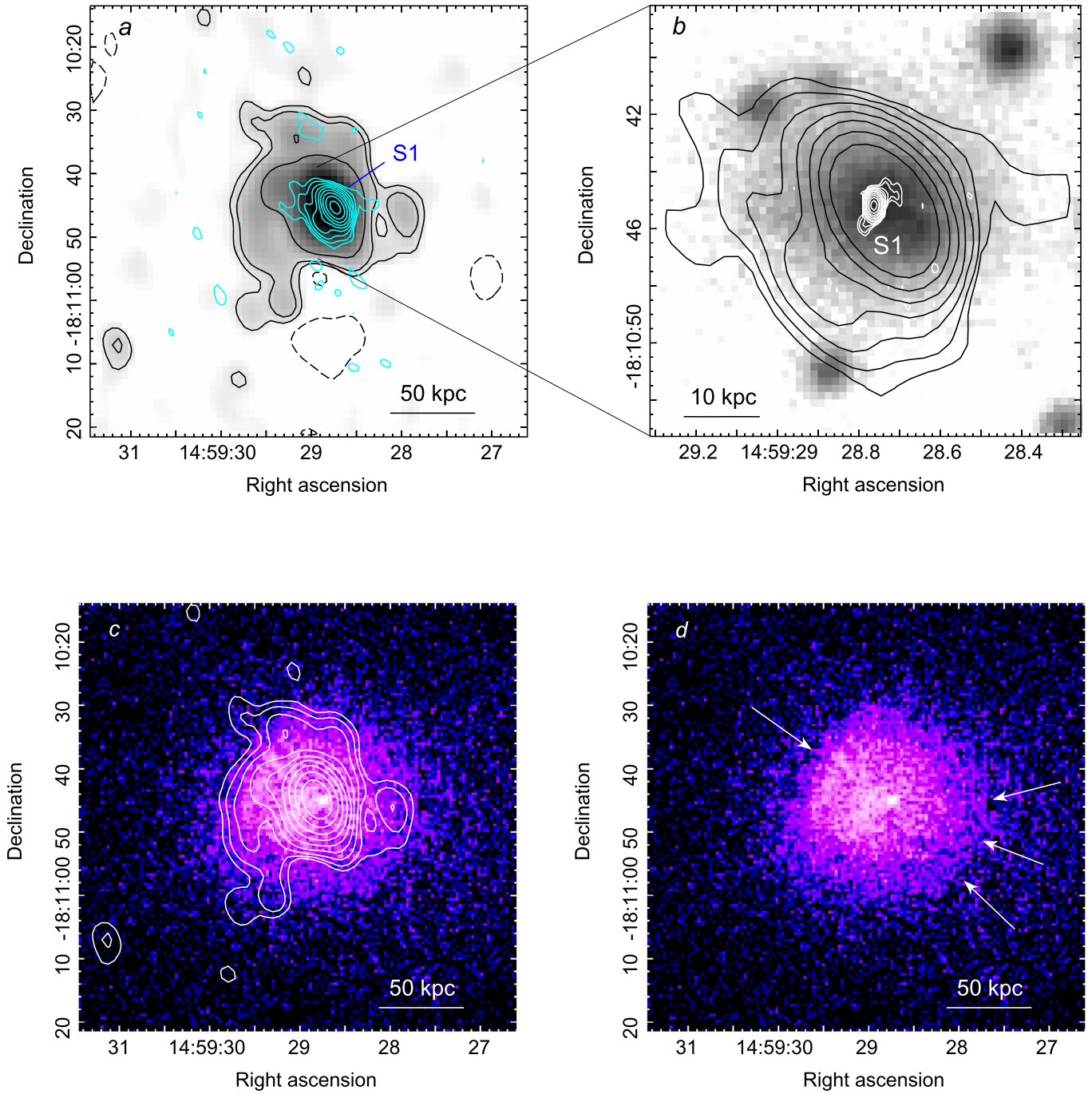

Figure 4. AS 780. (a) GMRT 1.30 GHz contours (cyan), overlaid on the GMRT image of the minihalo at 610 MHz (gray scale and black contours). The radio images have been restored with a $3'' \times 2''$ beam at 1.30 GHz and $6'' \times 4''$ at 610 MHz. Cyan contours start at $+3\sigma = 0.25$ mJy beam^{-1} and then scale by a factor of 2. Black contours are spaced by a factor of 2 between $3\sigma = 0.2$ and 1.6 mJy beam^{-1}. Contours at the -3σ level are shown as dashed. (b) VLA-A configuration contours at 8.46 GHz (white) of the cluster central radio galaxy S1 on the optical Pan-STARRS-1 r image. The angular resolution is $0\farcs4 \times 0\farcs3$. White contours start at $+3\sigma = 0.09$ mJy beam^{-1} and then scale by a factor of 2. Black contours show the radio emission detected by the GMRT at 1.30 GHz (panel ((a)) and are spaced by a factor of 2 between $+3\sigma = 0.25$ and 16 mJy beam^{-1}. (c) GMRT 610 MHz contours from panel (a), superposed on the *Chandra* X-ray image in the 0.5–4 keV band. Radio contours start at $+3\sigma = 0.2$ mJy beam^{-1} and then scale by a factor of 2. (d) *Chandra* X-ray image, same as panel (c). Arrows mark the positions of two possible cold fronts.

3.5. A3444

At $z = 0.254$, A3444 is a relaxed cluster with a central, low-entropy cool core (G17). A possible central minihalo was reported in this cluster by Venturi et al. (2007) based on GMRT images at 610 MHz. In Figure 5, we present our VLA images at 1.4 GHz compared to the cluster optical and X-ray emission. The BnA image (panel (a)) shows a central compact radio source (S1) fully enveloped by a roundish minihalo containing no jets. The unresolved source is associated with the BCG, and its size is <20 kpc. In a higher-resolution image from recent GMRT observations at 1.28 GHz (S. Giacintucci et al. 2019, in

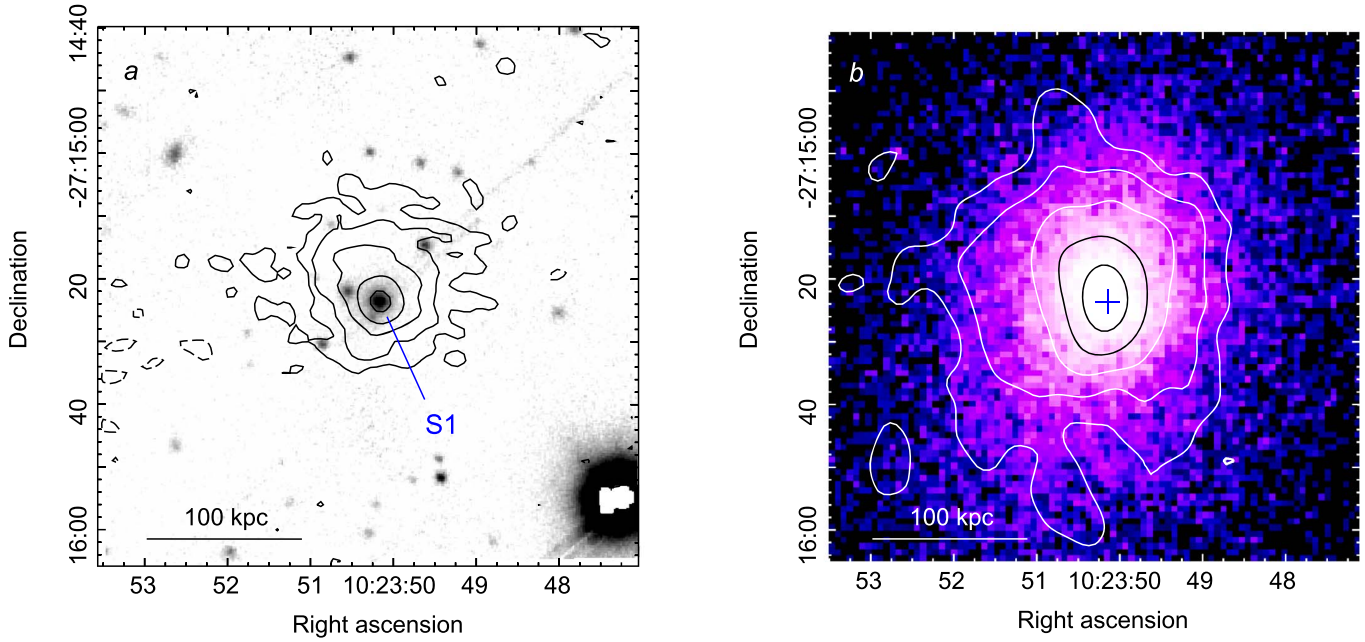

Figure 5. A3444. (a) VLA 1.4 GHz BnA-configuration image, restored with a 5″ circular beam and overlaid on the optical Pan-STARRS-1 *r* image. The rms noise is $1\sigma = 35$ μJy beam^{-1}. Contours start at 0.09 mJy beam^{-1} and then scale by a factor of 2. Contours at −0.09 mJy beam^{-1} are shown as dashed. The central radio galaxy is S1. (b) VLA 1.4 GHz combined DnC+BnA-configuration contours of the minihalo and central radio galaxy S1 (black cross), overlaid on the *Chandra* image in the 0.5–4 keV band. The radio image has been restored with an 11″ circular beam. The rms noise is $1\sigma = 45$ μJy beam^{-1}. Contours start at 0.13 mJy beam^{-1} and then scale by a factor of 2. No contours at a level of −0.13 mJy beam^{-1} are present in the part of the image shown.

preparation), the source is still pointlike, thus implying that its size must be even smaller (∼8 kpc or less). The minihalo size reaches a radius of ∼120 kpc in the combined DnC+BnA image in Figure 5(b). The flux density of S1 is $S_{1.4\,\mathrm{GHz}} = 1.41 \pm 0.07$ mJy, and its radio power $P_{\mathrm{BCG,1.4\,GHz}} = (0.28 \pm 0.01) \times 10^{24}$ W Hz^{-1}. The surrounding minihalo has $S_{1.4\,\mathrm{GHz}} = 12.1 \pm 0.9$ mJy and $P_{\mathrm{MH,1.4\,GHz}} = (2.38 \pm 0.17) \times 10^{24}$ W Hz^{-1}. A detailed spectral study of this minihalo, based on the VLA data presented here and new deep GMRT observations at 1.28 GHz and 610 MHz, will be presented in a future paper (S. Giacintucci et al. 2019, in preparation), where the spatial correlation between the radio and X-ray emission is also investigated.

4. New Minihalo Detections

Our analysis of the GMRT data of the clusters A907, A2667, and PSZ1 G139.61+24.20 (Table 2) led to the detection of large-scale diffuse emission in their cool cores, which we classify as minihalos. In the following sections, we describe these newly discovered minihalos and summarize their properties.

4.1. A907

We have reanalyzed an archival GMRT observation at 610 MHz (Table 2) of this relaxed, cool-core cluster at $z = 0.153$. In Figure 6(a), we present a 610 MHz image overlaid as contours on an optical *r*-band image from Pan-STARRS1. The figure shows a radio point source (S1) at the center of a region of diffuse emission, about 70 kpc in radius, that we classify as a minihalo. The source S1 is identified with the cluster dominant galaxy. An extended head–tail source (S2) is also visible in the image. No redshift information is available for this object; however, its radio morphology, typical of dense environments, suggests that it is a cluster member. Panel (b) shows a comparison of the radio and *Chandra* X-ray emission. The minihalo fills a large fraction of the central cool core and appears to be bounded by a pair of apparent X-ray cold fronts, as it is often observed in minihalo clusters with similar sloshing features in their cores.

We measure a flux density of $S_{610\,\mathrm{MHz}} = 117 \pm 9$ mJy for the central galaxy S1 and $S_{610\,\mathrm{MHz}} = 42 \pm 3$ mJy for S2. The minihalo has $S_{610\,\mathrm{MHz}} = 34.9 \pm 5.6$ mJy (Table 3). No high-resolution images at 1.4 GHz are available for this cluster. An estimate of the flux and radio luminosity at 1.4 GHz can be obtained by extrapolating the 610 MHz fluxes using a spectral index of $\alpha = 1.0 \div 1.3$ for the minihalo (e.g., G14a) and $\alpha = 0.6 \div 0.8$ for the central active radio galaxy (e.g., Condon 1992). We obtain $S_{1.4\,\mathrm{GHz}} = 13.5 \pm 2.8$ mJy for the minihalo, which corresponds to a radio power of $P_{\mathrm{MH,1.4\,GHz}} = (0.9 \pm 0.2) \times 10^{24}$ W Hz^{-1}. For the BCG, we estimate $S_{1.4\,\mathrm{GHz}} = 65 \pm 7$ mJy and $P_{\mathrm{BCG,1.4\,GHz}} = (4.1 \pm 0.4) \times 10^{24}$ W Hz^{-1} (Table 4).

4.2. A2667

At $z = 0.23$, A2667 is a relaxed cluster with a bright, cool core (Cavagnolo et al. 2009). We imaged the central region of the cluster using two high-resolution observations at 1.15 GHz from the GMRT archive (Table 2). We also reanalyzed GMRT data at 610 MHz from Venturi et al. (2008). Our images are presented in Figure 7 and compared with optical and X-ray images. Panel (a) shows an overlay of the radio contours from the combined 1.15 GHz data on the *HST* ACS image, revealing a bright unresolved radio source (S1) coincident with the cluster central galaxy and a second point source (S2) associated with a member galaxy ($z = 0.234$; Covone et al. 2006). The ATCA[13]

[13] Australia Telescope Compact Array.

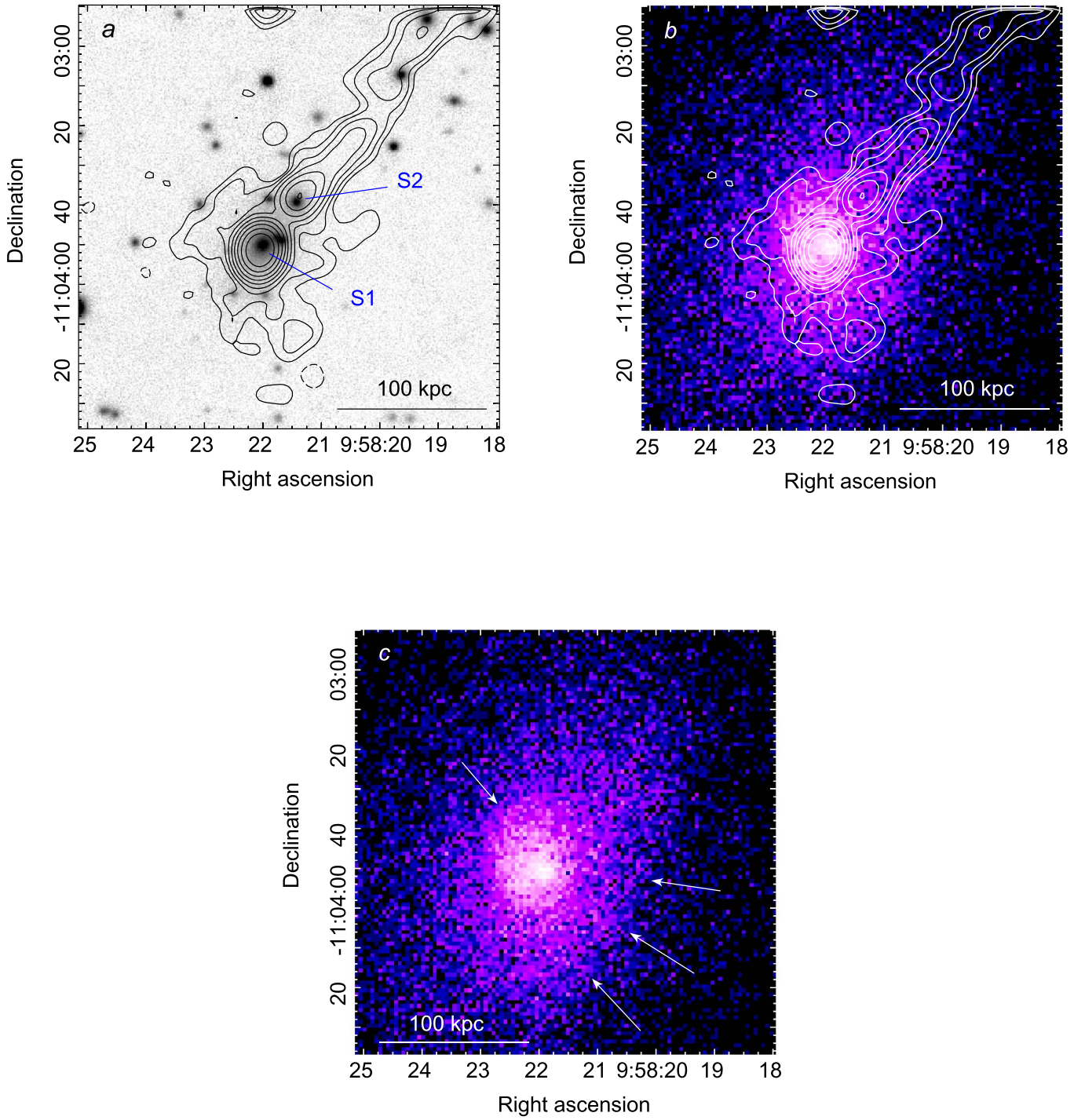

Figure 6. A907. (a) GMRT 610 MHz contours, overlaid on the optical Pan-STARRS-1 *r*-band image (gray scale). The radio image has been restored with a 5″ circular beam. The rms noise is $1\sigma = 40$ μJy beam^{-1}, and contours are spaced by a factor of 2 starting from 0.12 mJy beam^{-1}. Contours at -0.12 mJy beam^{-1} are shown as dashed. Here S1 is associated with the cluster central galaxy, and S2 is an extended, head–tail radio galaxy. (b) GMRT contours at 610 MHz, same as panel (a), overlaid on the *Chandra* X-ray combined image in the 0.5–2 keV band. (c) *Chandra* X-ray combined image, same as panel (b). Arrows mark the positions of two possible X-ray cold fronts.

observations at 4.8 and 8.6 GHz find S1 to be still unresolved at $\sim$1″ resolution (Hogan et al. 2015), thus limiting the spatial scale of any possible jets and/or lobes associated with the galaxy to $\sim$4 kpc or less. Diffuse radio emission that we classify as a minihalo is detected around S1. Panel (b) presents the radio contours at 610 MHz overlaid on the *Chandra* image, which is also shown in panel (c), with arrows marking the positions of two possible X-ray cold fronts. The minihalo covers an area of about 70 kpc in radius and appears to be contained within the sloshing region defined by the X-ray fronts.

The flux densities of S1 and S2 at 1.15 GHz and 610 MHz are summarized in Table 3. Their spectral indices are $\alpha = 0.5 \pm 0.1$ and 0.7 ± 0.1, respectively. We measure the minihalo flux

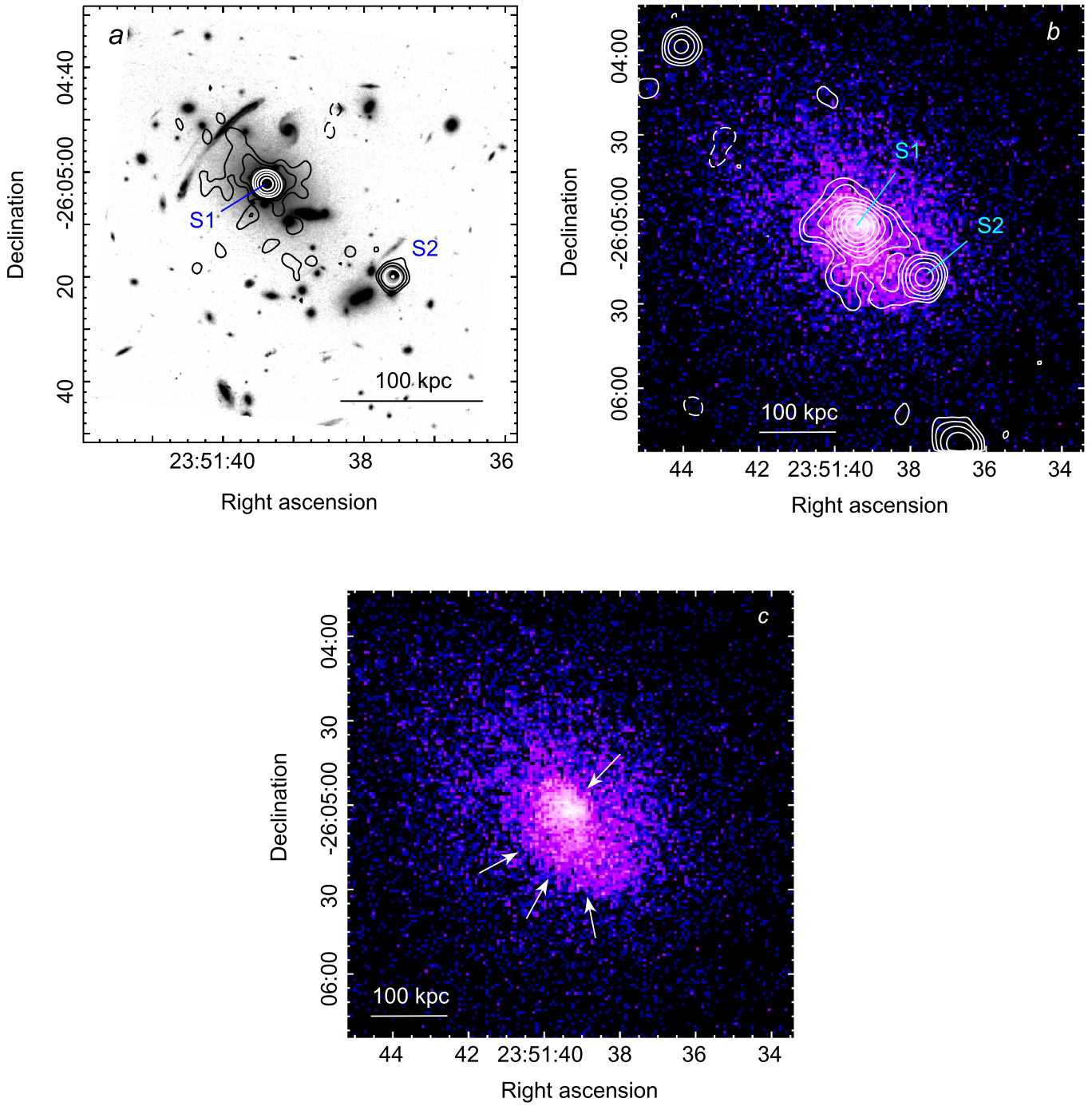

Figure 7. A2667. (a) GMRT 1.15 GHz contours, overlaid on the optical *HST* ACS image (gray scale). The radio image has been restored with a circular 2.″5 beam. The rms noise is $1\sigma = 35$ μJy beam^{-1}. Contours are scaled by a factor of 2, starting from 0.12 mJy beam^{-1}. Contours at -0.12 mJy beam^{-1} are shown as dashed. Individual radio galaxies are labeled. (b) GMRT contours at 610 MHz, overlaid on the *Chandra* X-ray image in the 0.5–4 keV band. The radio image has been restored with a circular 7″ beam. The rms noise is $1\sigma = 53$ μJy beam^{-1}. Contours are scaled by a factor of 2, starting from 0.16 mJy beam^{-1}. Contours at -0.16 mJy beam^{-1} are shown as dashed. Individual radio galaxies are labeled. (c) *Chandra* X-ray image, same as panel (b). White arrows indicate two surface brightness edges, which may be cold fronts.

density by subtracting the fluxes of S1 and S2 from the total emission. We obtain $S_{1.15\,\mathrm{GHz}} = 8.3 \pm 0.7$ and $S_{610\,\mathrm{MHz}} = 15.3 \pm 1.2$ mJy. A spectral index $\alpha = 1.0 \pm 0.2$ is inferred for the minihalo. Using this spectral index, we estimate a minihalo flux density at 1.4 GHz of $S_{1.4\,\mathrm{GHz}} = 7.1 \pm 0.6$ mJy and a luminosity of $P_{\mathrm{MH,1.4\,GHz}} = (1.1 \pm 0.1) \times 10^{24}$ W Hz^{-1} (Table 4). For the central galaxy, we estimate $S_{1.4\,\mathrm{GHz}} = 13.4 \pm 0.7$ mJy and $P_{\mathrm{BCG,1.4\,GHz}} = (2.1 \pm 0.1) \times 10^{24}$ W Hz^{-1} using $\alpha = 0.5 \pm 0.1$.

4.3. PSZ1 G139.61+24.20

At $z = 0.27$, PSZ1 G139.61+24.20 is a massive, cool-core cluster that was discovered by *Planck* (Planck Collaboration et al. 2014). We observed the cluster with the GMRT at

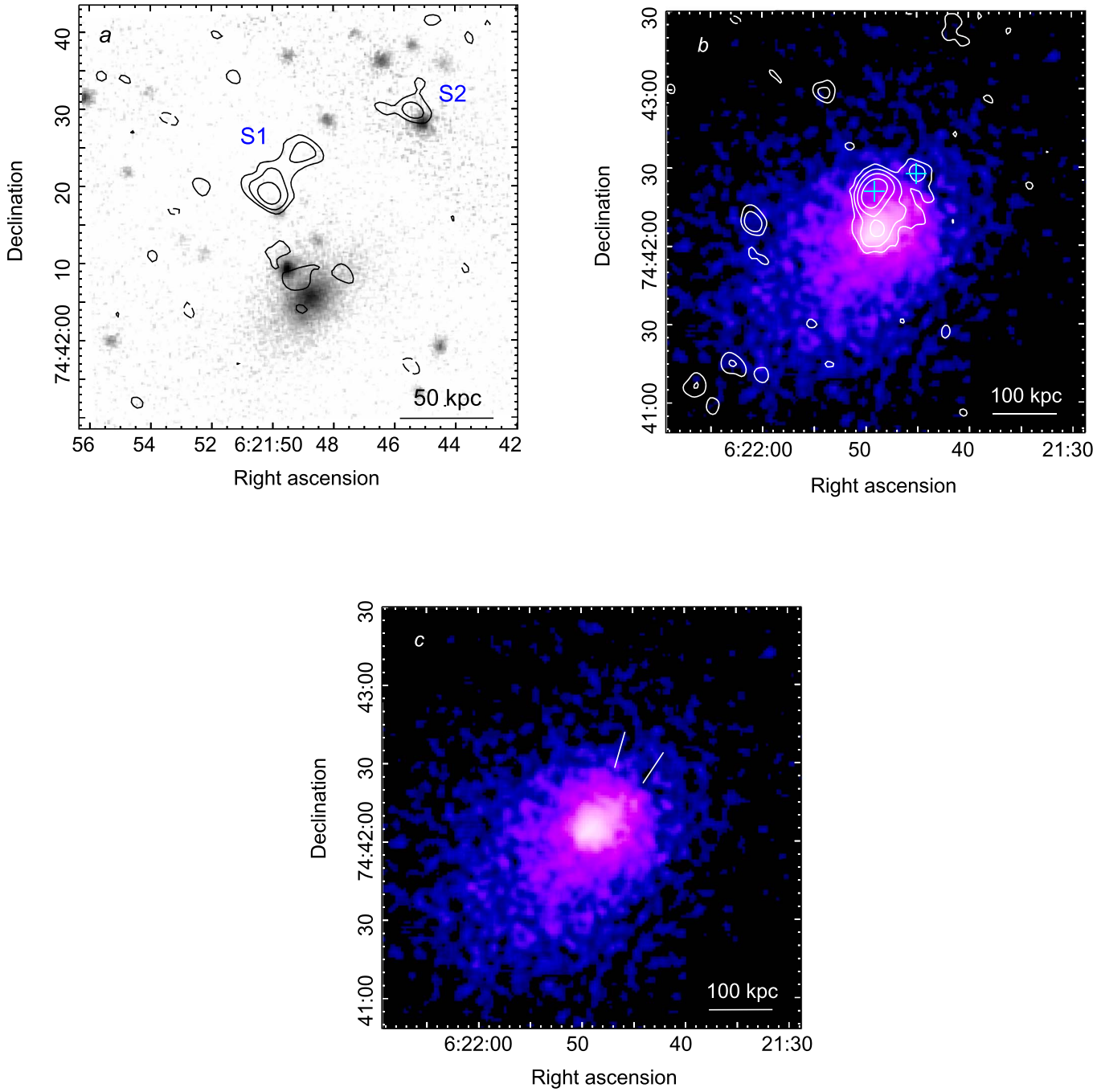

Figure 8. PSZ1 G139.61+24.20. (a) GMRT 1.28 GHz contours at a resolution of $3'' \times 2''$ in PA 53°, overlaid on the *r*-band Pan-STARRS1 optical image. The rms noise of the radio image is $1\sigma = 15$ μJy beam^{-1}. Contours are scaled by a factor of 2, starting from 0.05 mJy beam^{-1}. Contours at -0.05 mJy beam^{-1} are shown as dashed. Here S1 is an extended radio source with no optical identification on the POSS-II image, and S2 is a radio source with an optical counterpart. (b) Contours from the combined image at 610 MHz, restored with a $7''$ circular beam, overlaid on a *Chandra* smoothed X-ray image in the 0.5–4 keV band. The rms noise of the radio image is $1\sigma = 30$ μJy beam^{-1}. Contours are scaled by a factor of 2, starting from 0.08 mJy beam^{-1}. Crosses mark the positions of the radio galaxies S1 and S2 (panel (a)). (c) *Chandra* X-ray image, same as panel (b). White lines mark the position of an X-ray cold front (Savini et al. 2018).

1.28 GHz for approximately 5 hr and twice at 610 MHz for a total of 9.4 hr (Table 2). A high-resolution image at 1.28 GHz is shown as contours in Figure 8(a), compared to an optical *r*-band image from Pan-STARRS1. A 610 MHz image at $7''$ resolution is presented in Figure 8(b). At 1.28 GHz, hints of extended emission are visible at the location of the central optical galaxy, which lacks a clear radio counterpart. An extended double radio source (S1) is detected at $\sim 15''$ from the center. The source has no visible optical counterpart in the Pan-STARRS1 image, thus suggesting that it is a background, high-redshift radio galaxy. A second radio source (S2), located to the northwest, is associated with an optical galaxy with no redshift information.

At 610 MHz, the double source S1 blends with a central diffuse source with a size of $r \sim 50$ kpc that we classify as a minihalo (Figure 8(b)). An X-ray cold front, whose position is

marked by white lines in panel (c), was reported by Savini et al. (2018), indicating that the central cool gas is sloshing. The position of the cold front is roughly coincident with the northwestern boundary of the minihalo at 610 MHz, suggesting that its radio emission may be confined here by the front.

The minihalo has also been detected by Savini et al. (2018) at 610 MHz (using the same GMRT observations analyzed here) and at 144 MHz with LOFAR. The LOFAR image revealed the existence of a larger-scale diffuse component that surrounds the cool core and its central and more compact minihalo. This second component is undetected at higher frequencies, implying a very steep radio spectrum ($\alpha > 1.7$), and has been interpreted as an ultrasteep-spectrum radio halo similar to those found in unrelaxed clusters without a central cool core (e.g., Brunetti et al. 2008; Macario et al. 2010). Savini et al. argued that a recent cluster collision with a smaller subcluster may have perturbed the cluster on a large scale without destroying its central cool core and generated a large-scale radio halo. The same gravitational interaction may also have induced gas sloshing in the cool core and ensuing minihalo. This suggests that both a minihalo and a giant radio halo could at times coexist in the same cluster (Storm et al. 2015; Venturi et al. 2017; Savini et al. 2018; 2019; van Weeren et al. 2019).

The flux densities of S1 and S2 are summarized in Table 3, along with their spectral indices. For the minihalo, we estimated a flux density of $S_{610\,\mathrm{MHz}} = 2.3 \pm 0.8$ mJy. This value was obtained by subtracting the flux of S1 and S2, measured on the full 5″ resolution image (not shown here), from the total emission in Figure 8(b). At 1.28 GHz, we used a 5″ resolution image (not shown here) to measure the minihalo flux and obtained $S_{1.28\,\mathrm{GHz}} = 0.65 \pm 0.08$ mJy. A flux density of 12 mJy (with 15% uncertainty) is reported at 144 MHz by Savini et al. (2018). A spectral index of $\alpha = 1.33 \pm 0.08$ is inferred between 144 MHz and 1.28 GHz, consistent with the index in the 144–610 MHz range (Savini et al. 2018).

The flux density of the minihalo at 1.4 GHz, extrapolated from the lower-frequency measurements with $\alpha = 1.33 \pm 0.08$, is $S_{1.4\,\mathrm{GHz}} = 0.6 \pm 0.1$ mJy. The corresponding luminosity at 1.4 GHz is $P_{\mathrm{MH,1.4\,GHz}} = (1.3 \pm 0.2) \times 10^{23}$ W Hz^{-1} (Table 4). For the BCG, the nondetection at 1.28 GHz at a 3σ level of 0.035 mJy implies an upper limit to its 1.4 GHz radio power of $P_{\mathrm{BCG,1.4\,GHz}} < 7 \times 10^{21}$ W Hz^{-1} (adopting $\alpha = 0.6 \div 0.8$). We note that, to date, this is the only nondetection of radio emission from the BCG in a cluster that hosts a radio minihalo.

5. *Chandra* X-Ray Analysis

We use high angular resolution *Chandra* observations to map the X-ray-emitting gas in the cluster cores and compare its distribution to the radio minihalo images (Figures 3–6 and 10–16). In particular, we want to examine correlations of the minihalo radio luminosity at 1.4 GHz and the X-ray luminosity of whole clusters and their cores (Section 6). In the following subsections, we describe the analysis of the *Chandra* observations that we have used. They are listed in Table 5, along with clean exposure times and the adopted Galactic absorption column density N_{H} (discussed below).

5.1. Data Reduction

The Level-1 ACIS event files from the archive were reprocessed following the standard procedure (as described in Vikhlinin et al. 2005) using the *Chandra* Calibration Database (CALDB) 4.6.3. We excluded the background flare intervals and modeled the background as described in Markevitch et al. (2003). To model the detector + sky background, we used the CALDB blank-sky data sets appropriate for the date of each observation, projected to the sky and normalized using the ratio of the observed to blank-sky count rates in the source-free 9.5–12 keV energy band. Following Markevitch et al. (2000), we also subtracted the ACIS readout artifact (using the contributed tool make_readout_bg), which is particularly important in the presence of sharp X-ray brightness peaks in the clusters that we study here. We used images in the 0.5–4 and 2–7 keV energy bands to detect the unrelated point sources and small-scale extended sources. These sources were masked out from the spectral analysis.

For each cluster, we obtained a background-subtracted, exposure-corrected image in the 0.5–4 keV band. For clusters with multiple ACIS observations, we first coadded the individual background-subtracted images and then divided the count images by the sum of the corresponding exposure maps.

To derived the X-ray temperatures and luminosities, we extracted a spectrum of each cluster region of interest and generated the instrument responses (ARF and RMF) using calibration file versions N0008 for the telescope effective area, N0006 for the CCD quantum efficiency, and N0009 for the ACIS time-dependent contamination model. Background spectra were extracted for the same regions from the blank-sky data sets, normalized as described in Section 5.1. The cluster X-ray emission was modeled with an absorbed single-temperature APEC model in the 0.7–7 keV energy band, with the heavy-element abundance (same for all elements above He) relative to solar free to vary. The absorption column density N_{H} was initially allowed to vary; if the best-fit N_{H} value was found to be consistent with that from the Leiden/Argentine/Bonn (LAB) radio survey of Galactic H I (Kalberla et al. 2005), we then fixed it at the database value for subsequent analysis. Deviations from the radio survey values can be either real (because of nonuniformity of the column density on the cluster scale or additional molecular hydrogen) or caused by the residual inaccuracies of the ACIS contamination model. Using the best-fit N_{H} models such complications away and serves our purpose of deriving the cluster intrinsic X-ray luminosity and temperature. The choice of the lower-energy boundary of 0.7 keV further limits the importance of such deviations. The adopted N_{H} values are listed in Table 5.

For several clusters, we combined multiple *Chandra* observations by fitting their spectra separately but simultaneously, with the X-ray model parameters tied together but using separate detector responses. For RXC J1504.1–0248, for which the observations had the same pointing position and roll angle and thus the same responses, we instead coadded the spectra.

5.2. X-Ray Luminosities

For each cluster, we define three interesting regions: (1) the whole cluster, $r \leqslant R_{500}$; (2) the core region, $r \leqslant 0.15R_{500}$ (which is in the $r = 140$–240 kpc range for our clusters); and

Table 5
Chandra Observations Analyzed in This Work

Cluster Name	Observation ID	Detector (ACIS)	Exposure (ks)	$N_{\rm H}$ (10^{20} cm^{-2})
1	2	3	4	5
A478	1669	S	36.3	$31.03^{+0.18}_{-0.18}$
MACS J0159.8–0849	6106	I	35.3	2.06*
MACS J0329.6–0211	3582	I	19.7	4.64*
ZwCl 3146	9371	I	38.1	2.46*
RX J1532.9+3021	1665, 14009	I, S	9,88	2.30*
A2204	7940	I	76.7	$8.23^{+0.45}_{-0.39}$
Perseus	11715	I	70.5	13.6*
A1835	6880	I	119	2.04*
Ophiuchus	16627	I	35.0	$35.7^{+0.26}_{-0.25}$
A2029	4977, 6101	S, I	76.7, 9.3	3.25*
RBS 797	2202, 7902	I, S	11, 7 38.4	2.27*
RXC J1504.1–0248	17197, 17669, 17670	I	29.8, 28.5, 44.6	$14.35^{+4.6}_{-4.6}$
RX J1347.5–1145	14407	I	60.1	4.60*
RXC J1720.1+2637	4361	I	22.0	3.36*
MS 1455.0+2232	4192	I	91.2	3.18*
2A 0335+096	7939	S	49.8	$23.18^{+0.27}_{-0.24}$
A907	3185, 3205	I	47.7, 35.8	5.45*
A2667	2214	S	9.3	1.73*
RX J2129.6+0005	9370	I	29.8	3.64*
AS 780	9428	S	39.4	7.39*
A3444	9400	S	36.3	5.55*
PSZ1 G139.61+24.20	15139	I	17.9	$13.11^{+1.7}_{-1.6}$
Phoenix	16545	I	59.9	1.52*

Note. Column 1: cluster name; column 2: observation identification number; column 3: *Chandra* ACIS detector; column 4: total clean exposure; column 5: Galactic absorption column density adopted in this paper. Values marked with * are from LAB (Section 5.1).

(3) the central coolest core region, $r \leqslant 70$ kpc, which is within the cooling radius of all of our clusters. Here R_{500} was derived from the total cluster masses M_{500} estimated from the *Planck* Sunyaev–Zeldovich (SZ) signal, which are available for 17 out of 23 clusters (Table 6). For the remaining clusters (marked by a $\star$), we used a mass estimate from G17, which is based on the $M_{500}-T_{\rm X}$ relation of Vikhlinin et al. (2009), using X-ray-measured, core-excised ($r > 70$ kpc) temperatures.

For these three regions, we first determined an X-ray luminosity in the 0.1–2.4 keV band for each cluster. For 12 clusters in the sample, *Chandra* covered R_{500}, and we determined the luminosity by fitting the spectrum in the respective region and converting its normalization to luminosity (in the XSPEC package). For the 11 clusters marked with a † in Table 6, R_{500} was outside the *Chandra* field of view, so we adopted the 0.1–2.4 keV R_{500} luminosities from the Meta-Catalog of X-Ray Detected Clusters of Galaxies (MCXC; Piffaretti et al. 2011), which is mostly based on the *ROSAT* All Sky Survey (RASS). For A478 and Ophiuchus, we corrected the MCXC luminosities by factors of 1.34 and 1.25, respectively, to account for the different $N_{\rm H}$ derived from our *Chandra* fits, which were factors of 2.0 and 1.8 higher than the database values adopted for the RASS catalogs. This makes the luminosities internally consistent with those for the central regions that were derived directly from *Chandra* observations. For Perseus, even the $0.15R_{500}$ radius is not fully covered by one *Chandra* ACIS-I observation, so we used the *Chandra* mosaic from Aharonian et al. (2017) to derive the luminosity within $0.15R_{500}$.

To convert the 0.1–2.4 keV luminosities to the more physically meaningful bolometric ones, we need gas temperatures, which we have derived from *Chandra* spectral fits in the same regions for most clusters. The temperature fits are summarized in Table 6; their errors include the statistical uncertainty and a 10% uncertainty on the value of $N_{\rm H}$. For Perseus, Ophiuchus, and 2A 0335+096, *Chandra* coverage is too small to probe an average temperature within R_{500}, so we used average cluster temperatures from the literature instead, which come from instruments with a larger field of view (see Table 6). For Perseus and Ophiuchus, whose total mass is estimated from the $M_{500}-T_{\rm X}$ relation (the 2A 0335+096 mass comes from *Planck*), this should result in slightly underestimated masses and R_{500}, because the cool core biases the average temperature low. This will not affect our conclusions in any significant way. For a further eight clusters, marked with a ◊ in Table 6, the *Chandra* field of view is smaller than R_{500} but covers enough of it to derive a reliable temperature for the region, considering the steeply declining radial brightness profiles and the relatively small contribution of the missing emission to the spectrum. For these clusters, we use *Chandra* temperatures fitted in smaller regions given in the notes for Table 6. For Perseus, for simplicity, we used one ACIS-I pointing (Table 5) out of many available to derive a temperature for $r < 0.15R_{500}$, as it almost covers the whole region. The statistics of that data subset are more than sufficient. The above simplifications are adequate because we are using the temperatures only for the luminosity conversion.

For each cluster region, we converted the 0.1–2.4 keV luminosities to the bolometric luminosities (Table 6) using a conversion factor appropriate for the corresponding temperature (Böhringer et al. 2004). The luminosity errors in Table 6

Table 6
Properties of Cluster Hosts

Cluster Name	M_{500} ($10^{14}\ M_{\odot}$)	R_{500} (Mpc)	$T_{X,R_{500}}$ (keV)	$T_{X,\ 0.15R_{500}}$ (keV)	$T_{X,70\ kpc}$ (keV)	$L_{X,\ R_{500}}$ (10^{44} erg s^{-1})	$L_{X,\ 0.15R_{500}}$ (10^{44} erg s^{-1})	$L_{X,70\ kpc}$ (10^{44} erg s^{-1})
1	2	3	4	5	6	7	8	9
◊ † A478	$7.1^{+0.3}_{-0.4}$	1.3	6.4 ± 0.7	6.2 ± 0.6	5.2 ± 0.5	23.3 ± 3.0[a]	19.5 ± 2.3	7.8 ± 0.9
MACS J0159.8–0849	$6.9^{+0.9}_{-1.0}$	1.2	8.5 ± 0.5	7.5 ± 0.4	5.9 ± 0.3	40.6 ± 4.4	21.1 ± 2.2	9.6 ± 1.0
⋆ MACS J0329.6–0211[b]	4.9 ± 0.7	1.0	5.1 ± 0.3	5.1 ± 0.3	4.3 ± 0.3	27.2 ± 2.7	15.7 ± 1.7	9.5 ± 1.0
⋆ ZwCl 3146	6.7 ± 0.8	1.2	6.5 ± 0.1	5.9 ± 0.1	4.7 ± 0.1	45.6 ± 4.6	28.9 ± 3.0	13.8 ± 1.4
⋆ RX J1532.9+3021	4.7 ± 0.6	1.0	6.0 ± 0.3[c]	5.1 ± 0.1	4.5 ± 0.1	41.6 ± 4.5[c]	27.8 ± 2.8	15.9 ± 1.6
◊ † A2204	8.0 ± 0.4	1.3	6.6 ± 0.2	6.3 ± 0.2	5.1 ± 0.1	35.0 ± 3.8	25.1 ± 2.7	13.1 ± 1.3
⋆ † Perseus	6.1 ± 0.6	1.3	6.4 ± 0.1[d]	6.4 ± 0.2	4.1 ± 0.1	14.9 ± 1.5	10.4 ± 1.0[e]	4.4 ± 0.5
A1835	$8.5^{+0.5}_{-0.6}$	1.3	7.7 ± 0.1	6.9 ± 0.1	5.6 ± 0.1	56.5 ± 5.7	34.5 ± 3.5	16.8 ± 1.7
⋆ † Ophiuchus	12.4 ± 1.2	1.6	10.3 ± 0.2[d]	9.4 ± 0.1	8.8 ± 1.1	19.7 ± 2.0[f]	12.9 ± 1.3	3.0 ± 0.4
◊ † A2029	6.8 ± 0.2	1.3	8.1 ± 0.2[g]	7.5 ± 0.1[h]	6.6 ± 0.1[h]	24.3 ± 2.4	15.0 ± 1.5[h]	6.3 ± 0.6[h]
RBS 797	$6.3^{+0.6}_{-0.7}$	1.2	6.7 ± 0.3[i]	6.1 ± 0.1[j]	5.3 ± 0.1[j]	41.9 ± 5.4[i]	32.2 ± 3.2[j]	18.9 ± 1.9[j]
RXC J1504.1–0248	7.0 ± 0.6	1.3	5.9 ± 0.4	5.6 ± 0.4	4.9 ± 0.3	68.4 ± 7.0	52.1 ± 5.6	31.3 ± 3.3
RX J1347.5–1145	$10.6^{+0.7}_{-0.8}$	1.3	12.8 ± 0.5	12.7 ± 0.5	9.8 ± 0.4	147.3 ± 15.4	99.0 ± 10.0	40.9 ± 4.3
◊ † RX J1720.1+2638	6.3 ± 0.4	1.2	6.6 ± 0.1	6.1 ± 0.2	5.1 ± 0.1	17.2 ± 1.7	12.9 ± 1.3	6.2 ± 0.6
⋆ MS 1455.0+2232	3.5 ± 0.4	1.0	4.9 ± 0.1	4.8 ± 0.1	4.6 ± 0.1	21.1 ± 2.2	14.7 ± 1.5	8.6 ± 0.9
† 2A 0335+096	$2.3^{+0.2}_{-0.3}$	0.9	3.6 ± 0.1[k]	2.5 ± 0.1	2.3 ± 0.1	4.4 ± 0.5	3.4 ± 0.3	2.3 ± 0.2
◊ † A907	5.2 ± 0.5	1.2	5.8 ± 0.1	5.4 ± 0.1	4.8 ± 0.1	12.1 ± 1.6	7.0 ± 0.7	2.9 ± 0.3
◊ † A2667	6.8 ± 0.5	1.2	6.4 ± 0.2	5.5 ± 0.2	4.6 ± 0.2	28.8 ± 4.1	16.0 ± 1.7	6.2 ± 0.7
◊ † A3444	$7.6^{+0.5}_{-0.6}$	1.3	6.2 ± 0.2	5.7 ± 0.2	5.0 ± 0.2	28.3 ± 4.0	18.5 ± 1.9	8.9 ± 0.9
RX J2129.6+0005	4.2 ± 0.6	1.1	6.4 ± 0.2	6.1 ± 0.2	5.1 ± 0.2	21.1 ± 2.1	11.2 ± 1.1	5.5 ± 0.5
◊ † AS 780	7.7 ± 0.6	1.3	5.2 ± 0.2	4.7 ± 0.1	3.9 ± 0.1	30.0 ± 6.2	10.9 ± 1.1	5.9 ± 0.6
PSZ1 G139.61+24.20	7.1 ± 0.6	1.2	6.9 ± 0.5	7.2 ± 0.6	6.2 ± 0.5	25.2 ± 2.7	12.6 ± 1.4	5.6 ± 0.6
Phoenix	12.6 ± 2.0[l]	1.3	10.6 ± 0.4	10.0 ± 0.3	8.8 ± 0.4	143.7 ± 15.0	112.2 ± 11.3	62.6 ± 6.5

Notes. Column 1: cluster name. Column 2: total mass within R_{500} from Planck Collaboration et al. (2014). For clusters marked with a ⋆, M_{500} is from G17 and estimated from the M_{500}–T_X relation of Vikhlinin et al. (2009) using core-excised ($r > 70$ kpc) temperatures. Column 3: R_{500}, derived from M_{500}. Columns 4–6: cluster temperature measured within a radius corresponding to R_{500}, $0.15R_{500}$, and 70 kpc. For the clusters marked by a ◊, the total temperature was measured within a radius smaller than R_{500}. A478: $r = 315$ kpc; A2204: $r = 360$ kpc; A2029: $r = 390$ kpc; RX J1720.1+2638: $r = 860$ kpc; A907: $r = 930$ kpc; A2667: $r = 620$ kpc; A3444: $r = 600$ kpc; A S780: $r = 600$ kpc. Columns 7–9: bolometric X-ray luminosity measured within a radius corresponding to R_{500}, $0.15R_{500}$, and 70 kpc. For the clusters marked by a †, the R_{500} luminosity is from MCXC (see Section 5.2).

[a] The MCXC luminosity was increased by a factor of 1.34 to account for the different N_H used in our *Chandra* analysis.
[b] From ObsId 3582.
[c] From ObsId 1665.
[d] Ikebe et al. (2002).
[e] See Section 5.2.
[f] The MCXC luminosity was increased by a factor of 1.25 to account for the different N_H used in our *Chandra* analysis.
[g] From ObsId 6101.
[h] From ObsId 4977.
[i] From ObsId 2202.
[j] From ObsId 7902.
[k] David et al. (1993).
[l] McDonald et al. (2015).

include the uncertainty on the temperature and a 10% *ROSAT*–*Chandra* flux cross-calibration uncertainty, added in quadrature. The latter was evaluated by comparing the R_{500} 0.1–2.4 keV luminosities derived from *Chandra* and those determined from *ROSAT* for the 10 clusters in our sample with both the *Chandra* and the MCXC measurements. We found that our *Chandra* luminosities are, on average, 6% higher than the RASS ones, with a scatter of ∼10%.

6. Discussion

In this paper, we have presented new GMRT and VLA radio images of eight cool-core clusters. Our images confirm the presence of radio minihalos in three of these clusters that had minihalo candidates and previously known minihalos in two clusters and discover new minihalos in three clusters. For consistency with the present analysis and previous work (G14a; G17), we have also reanalyzed VLA 1.4 GHz archival observations of seven clusters with known minihalos (Appendix A). Below, we briefly summarize our main radio results.

1. Our GMRT images of MACS J0159.8–0849 (1.4 GHz), MACS J0329.6–0211, and RXC J2129.6+0005 (1.3 GHz) detail the radio emission in the cluster center on angular scales 2″ and up. This corresponds to a physical size of $\gtrsim$10 kpc (7 kpc for RXC J2129.6+0005). We do not detect any well-defined jets, lobes, or tails from the central AGN on this scale, which is considerably smaller than that of the surrounding diffuse minihalo seen in the lower-resolution images ($R_{MH} > 70$ kpc; G14a; K15). We thus confirm the presence of minihalos in these clusters (no morphological connection between the diffuse radio emission and the AGN).

2. We have presented new GMRT images at 1.28 GHz and 610 MHz of the minihalo in AS 780 (Venturi et al. 2017). The minihalo, which extends ∼50 kpc in radius, appears to be confined within a pair of prominent sloshing cold fronts seen in the *Chandra* image. Our reanalysis of an archival VLA observation at 8.46 GHz shows the cluster central galaxy to be a core-dominated, double-lobe radio source of 8 kpc in length with no morphological connection to the much larger minihalo.
3. We have presented VLA images at 1.4 GHz of the minihalo in A3444, first reported by Venturi et al. (2007). The diffuse emission covers the central $r \sim 120$ kpc region of the cluster core and encloses a weak compact source ($\lesssim$8 kpc) associated with the BCG. In a forthcoming paper (S. Giacintucci al. 2019, in preparation), we will present new, deep GMRT observations at 1.28 GHz and 610 MHz, study the radio spectral properties of the minihalo, and investigate a possible spatial correlation between the radio and X-ray emission.
4. Using GMRT observations, we have detected new minihalos in the cores of A2667, A907, and PSZ1 G139.61+24.20. For the latter, a recent LOFAR observation at 144 MHz has shown the central minihalo to be surrounded by a larger-scale and fainter diffuse component, with a much steeper radio spectrum (Savini et al. 2018)—perhaps another example of minihalo-like emission inside a giant radio halo, as possibly seen in A2319 (Storm et al. 2015), A2142 (Venturi et al. 2017), and RX J1720.1+2638 (Savini et al. 2019).

With the new minihalo detections and candidate verifications presented in this work, the total number of confirmed minihalos has now increased to 23 (Table 4). This allows us to revisit some correlations between nonthermal emission and the thermal properties of the minihalo cluster hosts. We will consider some other correlations in the forthcoming work.

6.1. Radio Minihalos and Properties of the Cluster Hosts

A possible intrinsic relation between the nonthermal and global thermal properties of clusters with a central minihalo has been suggested by early works, based on a small number of minihalos ($\lesssim$10; e.g., Cassano et al. 2008; Kale et al. 2013). More recently, K15 and Gitti et al. (2018) used a larger sample of minihalos to investigate the distribution of minihalo clusters in the $P_{\rm MH,1.4\ GHz}$–$L_{\rm X}$ plane and reported a positive correlation. The physical origin of this correlation might be a correlation of the radio power with the total cluster mass, as found for the giant radio halos (e.g., Cassano et al. 2013), because the cluster mass and X-ray luminosity correlate. However, in G14a, we did not find evidence for a correlation with the mass for 14 minihalos with available masses from the *Planck* SZ observations. We also did not find a strong correlation between the radio power and the cluster core-excised X-ray temperature, which is a better proxy for the cluster total mass than the X-ray luminosity (e.g., Vikhlinin et al. 2009).

With our new minihalo detections, we can explore these possible correlations further. Our statistical analysis will include 22 confirmed minihalos, excluding AS 780, which has only a lower limit for the minihalo 1.4 GHz luminosity, but we show it in the plots. To evaluate the presence of any possible correlation and its strength, we use the Spearman's test, which computes a rank correlation coefficient, r_s, whose value can range from –1 (perfect anticorrelation) through zero (no correlation) to 1 (perfect correlation). The test also returns the probability *probrs* to get the observed r_s value by chance under the null hypothesis of no correlation (false positive). In Table 7, we summarize the values of r_s and *probrs* found for the relations analyzed in the following paragraphs.

Table 7
Spearman's Rank Correlation Coefficient Test

Relation	r_s	*probrs*
1	2	3
$P_{\rm MH,1.4\ GHz}$–M_{500}	+0.06	79%
$P_{\rm MH,1.4GHz}$–$L_{{\rm X},R_{500}}$	+0.53	11%
$P_{\rm MH,1.4GHz}$–$L_{{\rm X},\ 0.15R_{500}}$	+0.56	6%
$P_{\rm MH,1.4GHz}$–$L_{\rm X,70\ kpc}$	+0.67	0.7%
$P_{\rm MH,1.4GHz}$–($L_{{\rm X},\ R_{500}}$ –$L_{\rm X,70\ kpc}$)	+0.44	4%
* $P_{\rm MH,1.4GHz}$–($L_{{\rm X},\ R_{500}}$ –$L_{{\rm X},\ 0.15R_{500}}$)	+0.43	4%
$P_{\rm MH,1.4GHz}$–$P_{\rm BCG,1.4GHz}$	+0.43	5%

Note. Column 1: relation (Figure 9; * figure not shown). Column 2: Spearman's rank correlation coefficient, a nonparametric measure of the statistical dependence between two variables. Column 3: probability of uncorrelated quantities producing data sets that have a Spearman correlation at least as extreme as the one computed from these data sets.

6.1.1. Radio Luminosity–Cluster Mass

In Figure 9(a), we compare the radio luminosity (Table 4) and the total cluster mass within R_{500} (Table 6) for our 23 minihalo clusters. The distribution in this plot is scattered, and no obvious correlation is visible. The Spearman test gives a rank correlation coefficient of $r_s = 0.06$ and $probrs = 0.79$, which indicates a lack of correlation with the cluster mass, consistent with the G14a finding from a smaller sample.

6.1.2. Luminosity Relations

In line with previous studies (e.g., Gitti et al. 2018), we find a positive correlation ($r_s = 0.53$) between the minihalo radio power and cluster total X-ray bolometric luminosity measured within R_{500} (Figure 9(b)). In cool-core clusters, such as the minihalo hosts, a large fraction of the total X-ray luminosity is found to arise from the central $0.15R_{500}$ region (e.g., Maughan et al. 2012), which is also the region where the minihalo is located. It is therefore interesting to check if the correlation seen in Figure 9(b) is driven by a correlation with the X-ray luminosity of the cluster core. In Figures 9(c) and (d), we compare the minihalo radio power to the X-ray bolometric luminosity measured within the central $r = 0.15R_{500}$ (which is in the $r = 140$–240 kpc range for our clusters) and the smaller $r = 70$ kpc regions, respectively.

The plot with the $0.15R_{500}$ X-ray luminosity (c) is rather similar to the plot with the total X-ray luminosity (b), and we find a similar rank correlation coefficient, $r_s = 0.56$. This is not surprising, since for our sample of strongly peaked clusters, the core/total luminosity ratio, $L_{\rm X,\ 0.15R_{500}}/L_{\rm X,R_{500}}$, ranges from 0.4 (AS 780) to 0.8 (A478), with an average value of 0.6. Thus, the central $r = 0.15R_{500}$ core region is the dominant contributor to the cluster total luminosity for most clusters in our sample, explaining the similarity of panels (b) and (c).

In Figure 9(d), we cut an even smaller region of the core and plot the radio luminosity versus the X-ray bolometric

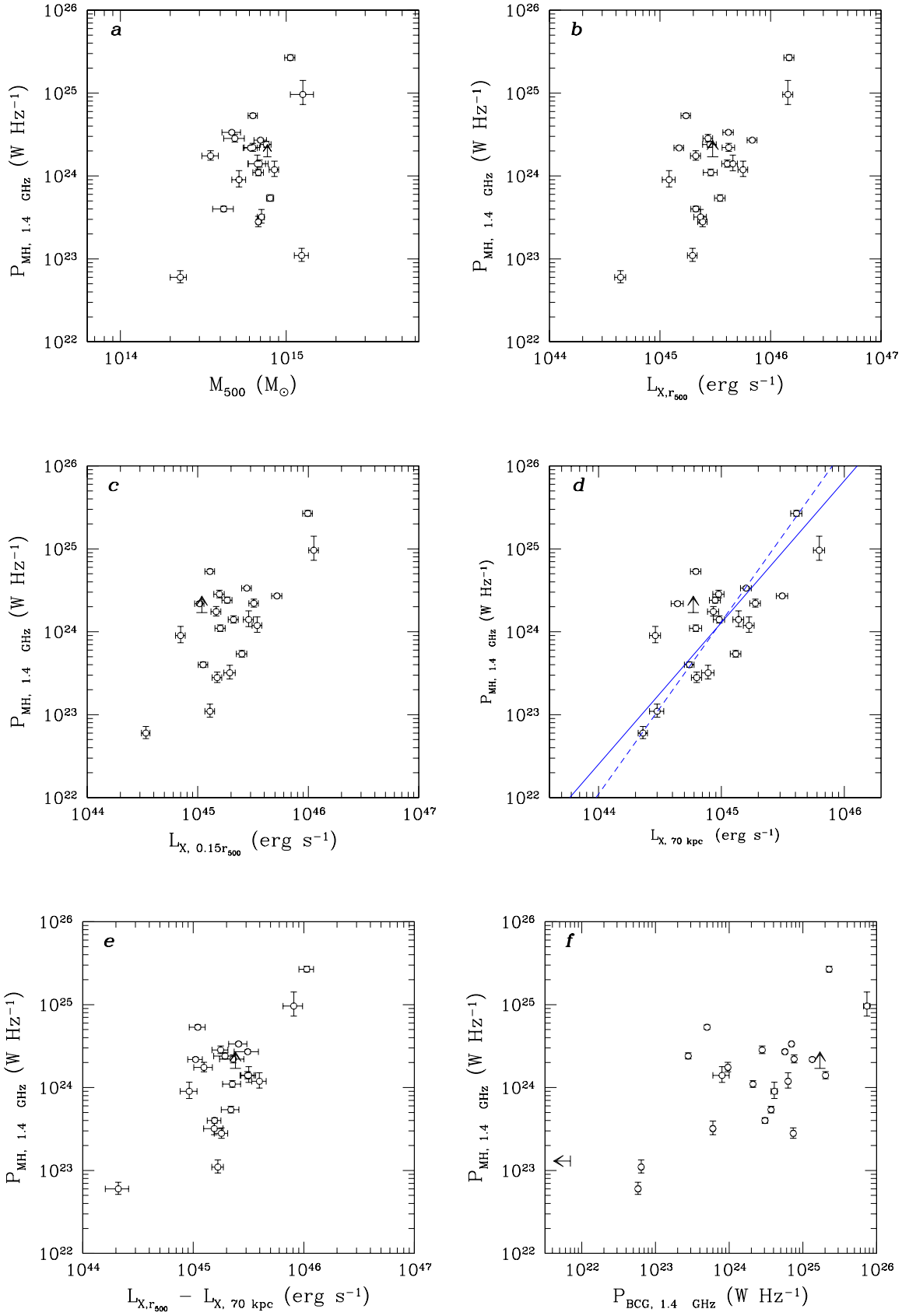

Figure 9. (a) Comparison between the 1.4 GHz radio luminosity of minihalos and total mass within R_{500} of their cluster hosts. (b)–(d) Comparison between the 1.4 GHz radio luminosity of minihalos and the cluster X-ray bolometric luminosity within (b) R_{500}, (c) $0.15R_{500}$, and (d) $r = 70$ kpc. Blue lines in panel (d) are the best-fit relations derived using the BCES bisector (solid line) and orthogonal (dashed line) regression algorithms (Equation (1)). (e) The minihalo 1.4 GHz luminosity is compared to the core-excised X-ray bolometric luminosity, a proxy for the cluster mass. (f) Comparison between the 1.4 GHz luminosity of minihalos and the BCG.

luminosity within the central $r = 70$ kpc, which is within the cooling radius for all of our clusters. This correlation is tighter, with a higher correlation coefficient, $r_s = 0.67$. The probability of the null hypothesis is less than 1%. For this relation, we also show the best-fit correlations in the form

$$\log(P_{\rm MH,1.4\,GHz}/10^{24}) = B \times \log(L_{\rm X,\,70\,kpc}/10^{44}) + A, \quad (1)$$

derived by implementing the bivariate correlated error and intrinsic scatter (BCES) bisector (blue solid line) and orthogonal (blue dashed line) regression algorithms (Akritas & Bershady 1996). The best-fit parameters are $A = -1.60 \pm 0.23$ and $B = 1.71 \pm 0.21$ (bisector) and $A = -1.96 \pm 0.31$ and $B = 2.08 \pm 0.34$ (orthogonal).

In Figure 9(e), we plot the radio luminosity as a function of the core-excised ($r > 70$ kpc) X-ray bolometric luminosity within R_{500}, which can be used as a proxy for the cluster total mass. This relation is weaker, with a correlation coefficient of $r_s = 0.44$, in agreement with the lack of strong scaling with the SZ-estimated cluster mass (panel (a)). A similar diagram (not shown here) is obtained if we excise the central $0.15R_{500}$ region instead of the smaller $r = 70$ kpc region, with a similar Spearman correlation coefficient and null-hypothesis probability (Table 7).

Finally, in Figure 9(f), we compare the radio luminosity of the minihalo to the radio luminosity of the central BCG (Table 4). A possible trend is visible, in line with previous analysis by Govoni et al. (2009) and G14a, but it is relatively weak ($r_s = 0.43$, $probs = 5\%$[14]), indicating that the AGN activity and minihalo emission are not tightly correlated. Interestingly, this correlation is weaker than that with the $r < 70$ kpc core X-ray luminosity, suggesting that the properties of the core gas may have a more direct effect on the minihalos than the AGN output.

Our minihalo sample is not statistically complete. Analysis of selection effects is beyond the scope of this paper; however, we checked for the possibility of the luminosity–luminosity correlations being dominated by effects originating from flux selection. The corresponding radio flux–X-ray flux diagrams show strong positive correlations reflecting the large range of distances but do not show any obvious flux-selection effects. This does not affect our main result of a better correlation of the minihalo radio power with the cool-core luminosity compared to the total luminosity, which is derived from the same sample and thus not driven by selection effects.

Our finding of a significant correlation between the minihalo radio power and the X-ray luminosity of the cool core is consistent with earlier findings by Gitti et al. (2004) and Bravi et al. (2016), who considered a correlation with the "cooling flow power"—which, by their derivation, is very close to the X-ray luminosity of the cooling region. Since we know that some physical process in the cluster cores compensates for X-ray radiative cooling (e.g., McNamara & Nulsen 2012), that process has to have a power very similar to the X-ray bolometric luminosity of the core, which is what cools the gas. Among the popular processes are the turbulence generated by AGN activity (Zhuravleva et al. 2014) and cosmic rays generated by the AGN (e.g., Guo & Oh 2008; Pfrommer 2013; Yang & Reynolds 2016; Ruszkowski et al. 2017). A further process is gas sloshing, which can provide a net heat inflow by bringing the outer, higher-entropy gas into the cool core (ZuHone et al. 2010). It is possible to make the conjecture that the same heating process is responsible for the radio minihalos. However, in addition to the minihalo power, any such hypothesis would need to explain other properties of the minihalos, in particular, their apparent close relation to the sloshing cold fronts (e.g., Mazzotta & Giacintucci 2008; ZuHone et al. 2013; Giacintucci et al. 2014a).

[14] The test was done using 21 minihalos: in addition to AS 780, we also excluded PSZ1 G139.61+24.20, which has only a lower limit for the BCG luminosity at 1.4 GHz.

7. Summary and Conclusions

We have presented new GMRT and *VLA* images of eight cool-core clusters. We have found new minihalos in A2667, A907, and PSZ1 G139.61+24.20; confirmed the minihalo candidates in MACS J0159.8–0849, MACS J0329.6–0211, and RXC J2129.6+0005; and presented new radio images of the previously known minihalos AS 780 and A3444. For consistency with our radio analysis, we have also reanalyzed archival VLA 1.4 GHz observations of seven cool-core clusters with known minihalos. Combining our new detections and confirmations with the previously known minihalos results in a total sample of 23 confirmed minihalos, the largest sample to date. We revisited possible correlations between nonthermal emission and thermal properties of their cluster hosts. We confirmed the lack of a strong relation between the minihalo radio power and the total cluster mass. Instead, we found a relatively strong positive correlation between the minihalo radio power and the X-ray bolometric luminosity of the cool core ($r < 70$ kpc). This supplements our earlier finding (G17) that most, if not all, cool cores in massive clusters contain radio minihalos. In many cases, we observe that the minihalo may be confined by the sloshing cold fronts in the core gas. Taken together, these findings suggest that the origin of the minihalos should be closely related to the properties of the cool-core gas.

Basic research in radio astronomy at the Naval Research Laboratory is supported by 6.1 Base funding. R.K. acknowledges support through the DST-INSPIRE Faculty Award by the Government of India. We thank the staff of the GMRT that made these observations possible. The GMRT is run by the National Centre for Astrophysics of the Tata Institute of Fundamental Research. The National Radio Astronomy Observatory is a facility of the National Science Foundation operated under cooperative agreement by Associated Universities, Inc.

Appendix A
Radio Observations and Images

Table 8 lists the VLA 1.4 GHz archival observations of seven clusters with known minihalos that we have reanalyzed in this work. The data were reduced as described in Section 2.2. The radio images are presented in Figures 11–16, compared to the X-ray *Chandra* and *XMM-Newton* images. In Table 9, we summarize for each cluster the flux density of the discrete radio galaxies detected in the area occupied by the minihalo and the source-subtracted flux density of the minihalos, measured as described in Section 2.1. A brief description of each individual cluster is given below.

A.1. Notes on Individual Clusters

A1835. A central minihalo was reported by Govoni et al. (2009). Our images are presented in Figure 10. The identification of the discrete sources embedded in the minihalo emission was done using the B-configuration image, shown in panel (a).

Table 8
Newly Analyzed 1.4 GHz VLA Observations

Cluster	Project	Configuration	Bandwidth (MHz)	Date	Time (minutes)	FWHM, PA (arcsec × arcsec, deg)	rms (μJy b^{-1})
1	2	3	4	5	6	7	8
A1835	AI75	B	25	1998 Jul 13	443	5.2 × 4.5, −74	15
	AG729	C	25	2006 Oct 23, 28	325	16.2 × 13.6, 37	30
	AG639	D	50	2003 Mar 11	260	50.5 × 45.0, 4	40
Ophiuchus	AC261	D	25	1990 Jan 25	28	91.6 × 39.2, −25	100
A2029	AL77	B	12.5	1984 Jan 15	69	4.5 × 4.3, 11	60
	AG729	C	50	2006 Dec 26	355	15.2 × 13.7, −15	30
	AG639	D	50	2003 Mar 09	293	57.3 × 45.2, 0	40
RBS 797	AS720	A	50	2002 Mar 27	257	1.6 × 1.2, −11	17
	AS720	B	50	2002 Jul 27	45	5.2 × 3.9, 10	27
RX J1347.5–1145	AS632	A	25	1998 Apr 22	115	1.7 × 1.3, −18	35
	AD511	C	50	2005 Sep 03	94	16.4 × 13.0, −1	40
MS 1455.0+2232	AL317	A	50	1994 Mar 12	33	1.5 × 1.2,33	55
	AS823	C	50	2006 Dec 12	31	16.5 × 14.6, −7	70
2A 0335+096	AM828	B	6.3	2005 Apr 29	136	4.2 × 3.9, −53	60
	AS465	C	50	1992 Mar 14	165	15.0 × 14.3, −39	38
	AS465	D	50	1992 Jul 14	117	50.9 × 45.2, 40	50

Note. Column 1: cluster name. Columns 2 and 3: VLA array configuration and project. Columns 4–6: observing bandwidth and date. Column 7: observing time. Column 8: radio beam (for ROBUST = 0 in IMAGR). Column 9: image rms level (1σ).

Table 9
Flux Densities of the Discrete Radio Sources and Minihalos

Cluster	Source	$S_{1.4\ \mathrm{GHz}}$ (mJy)	Cluster	Source	$S_{1.4\ \mathrm{GHz}}$ (mJy)
1	2	3	4	5	6
A1835	S1	32.4 ± 1.6	A2029	S1	513 ± 26
	S2	1.4 ± 0.1		S2	3.3 ± 0.2
	S3	1.7 ± 0.1		S3	1.3 ± 0.1
	S4	0.40 ± 0.02		S4	0.45 ± 0.02
	S5	0.55 ± 0.03		S5	0.31 ± 0.02
	S6	0.56 ± 0.03		S6	0.38 ± 0.02
	S7	0.14 ± 0.01		S7	4.3 ± 0.2
	S8	0.56 ± 0.03		S8	0.89 ± 0.04
	S9	0.63 ± 0.03		S9	6.6 ± 0.3
	S10	1.6 ± 0.1		S10	0.39 ± 0.02
	S11	0.67 ± 0.03		S11	0.30 ± 0.02
	S12	0.30 ± 0.02		MH	19.5 ± 2.5
	S13	3.3 ± 0.2			
	S14	0.21 ± 0.01	RBS 797	S1	17.9 ± 0.9
	S15	0.12 ± 0.01		MH	5.2 ± 0.6
	S16	0.15 ± 0.01			
	S17	0.14 ± 0.01	RX J1347.5–1145	S1	30.3 ± 1.5
	MH	6.1 ± 1.3		S2	4.9 ± 0.2[a]
				MH	35.6 ± 2.9
Ophiuchus	S1	30.6 ± 1.5			
	S2	1.8 ± 0.1	MS 1455.0+2232	S1	4.7 ± 0.2
	S3	24.5 ± 1.2		MH	8.5 ± 1.1
	S4	60.6 ± 3.0			
	S5	3.4 ± 0.2	2A 0335+096	S1	17 ± 1
	S6	5.2 ± 0.3		S2	1.0 ± 0.1
	S7	6.7 ± 0.3		MH	21.1 ± 2.1
	S8	593 ± 30			
	S9	4.7 ± 0.2			
	S10	3.3 ± 0.2			
	MH	62 ± 9			

Note. Column 1: cluster name. Column 2: radio source name. Column 3: flux density at 1.4 GHz.
[a] Measured on the C-configuration image; its flux density on the A-configuration image is 2.0 ± 0.1.

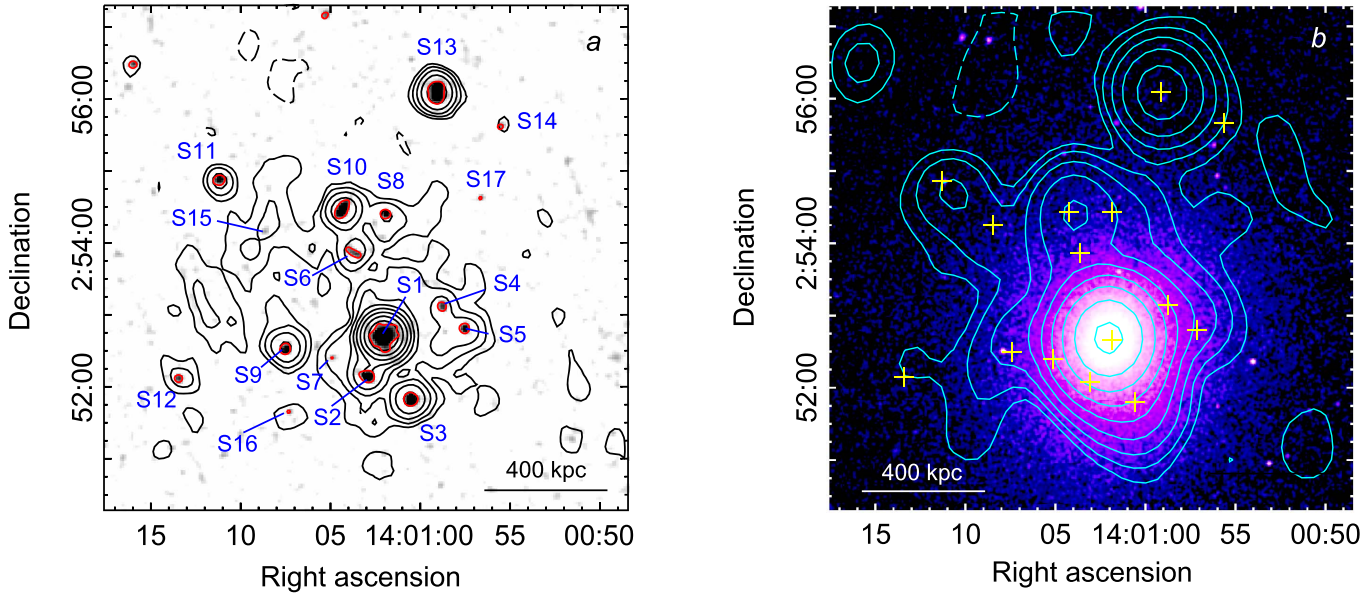

Figure 10. A1835. (a) VLA 1.4 GHz C-configuration contours at 20″ resolution (black), overlaid on the 1.4 GHz B-configuration image (gray scale and red contours) at 5″ resolution. The rms noise levels are $1\sigma = 30$ and 15 μJy beam^{-1}, respectively. Black contours are -1 (dashed), 1, 2, 4, 8, 16, . . .$\times$ 3σ. Red contours are at +5σ. Individual discrete radio sources are labeled. (b) VLA 1.4 GHz D-configuration contours of the minihalo and embedded radio sources (yellow crosses; see panel (a)), overlaid on the *Chandra* X-ray image in the 0.5–4 keV band. The radio image has a restoring beam of 51″ $\times$ 50″. The rms noise is $1\sigma = 40$ μJy beam^{-1}. Contours are -1 (dashed), 1, 2, 4, 8, 16, . . .$\times$ 2.5σ.

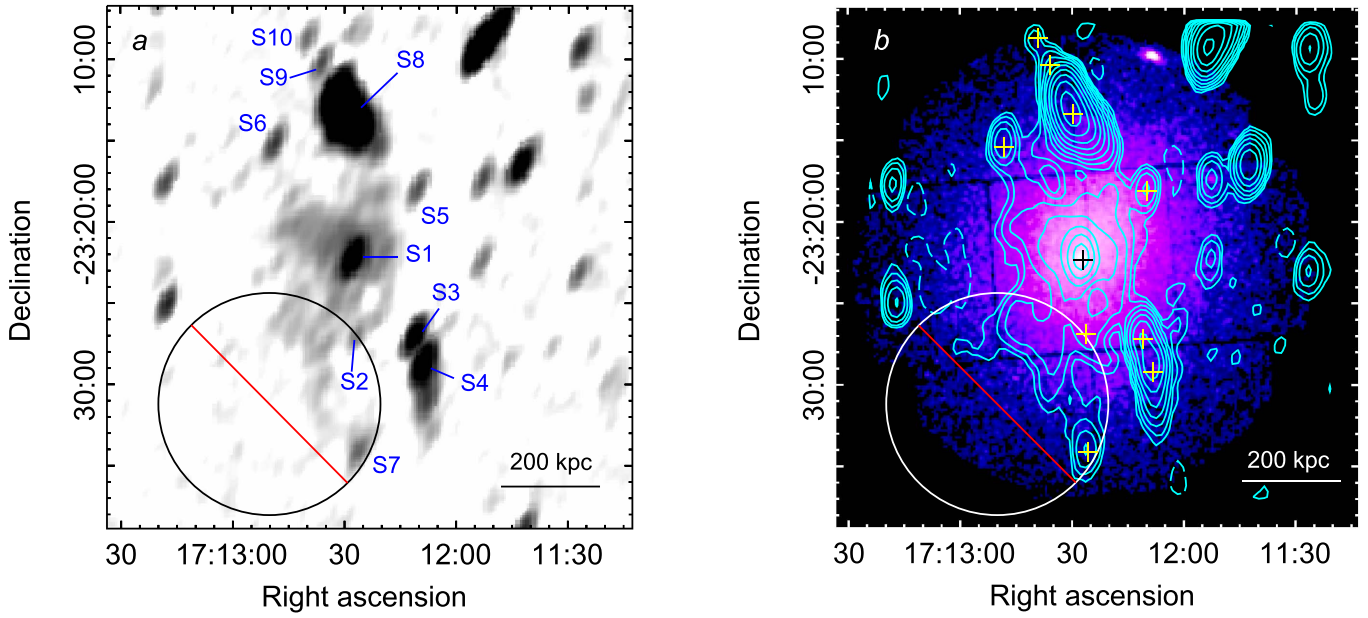

Figure 11. Ophiuchus. (a) VLA 1.4 GHz D-configuration image. The restoring beam is 92″ $\times$ 39″, and the rms noise is $1\sigma = 100$ μJy beam^{-1}. The individual radio galaxies are labeled. (b) VLA 1.4 GHz D-configuration contours of the minihalo and radio galaxies (yellow and black crosses; see panel (a)), overlaid on the *XMM-Newton* X-ray image (ObsID 0505150101). The radio image has a restoring beam of 110″ $\times$ 60″. The rms noise is $1\sigma = 120$ μJy beam^{-1}. Contours are -1 (dashed), 1, 2, 4, 8, 16, . . .$\times$ 2.5σ. The region associated with the low-frequency relic lobe that fills a possible X-ray cavity (circle; S. Giacintucci et al. 2019, in preparation) has been excluded to measure the flux density of the minihalo.

We identified 17 discrete sources above a $5\sigma = 0.075$ mJy beam^{-1} level (Table 9), accounting for a total of $S_{1.4\,\mathrm{GHz}} = 44.8$ mJy. A global flux of $S_{\mathrm{tot,1.4\,GHz}} = 50.6 \pm 2.5$ mJy is measured on the D-configuration image in the region occupied by the minihalo (Figure 10(b)). After subtraction of the flux in discrete sources, $S_{\mathrm{MH,1.4\,GHz}} = 6.1 \pm 1.3$ mJy remains for the minihalo, corresponding to a radio luminosity at 1.4 GHz of $P_{\mathrm{MH,1.4\,GHz}} = (1.19 \pm 0.25) \times 10^{24}$ W Hz^{-1}. Our flux value is in agreement with the flux density reported by Govoni et al. (2009) using the same C- and D-configuration observations analyzed here. The flux of the BCG is $S_{\mathrm{BCG,1.4\,GHz}} = 32.4 \pm 1.6$ mJy, and its radio power is $P_{\mathrm{MH,1.4\,GHz}} = (6.3 \pm 0.3) \times 10^{24}$ W Hz^{-1}.

Ophiuchus. A central minihalo was reported by Govoni et al. (2009) and Murgia et al. (2010). Our images are presented in

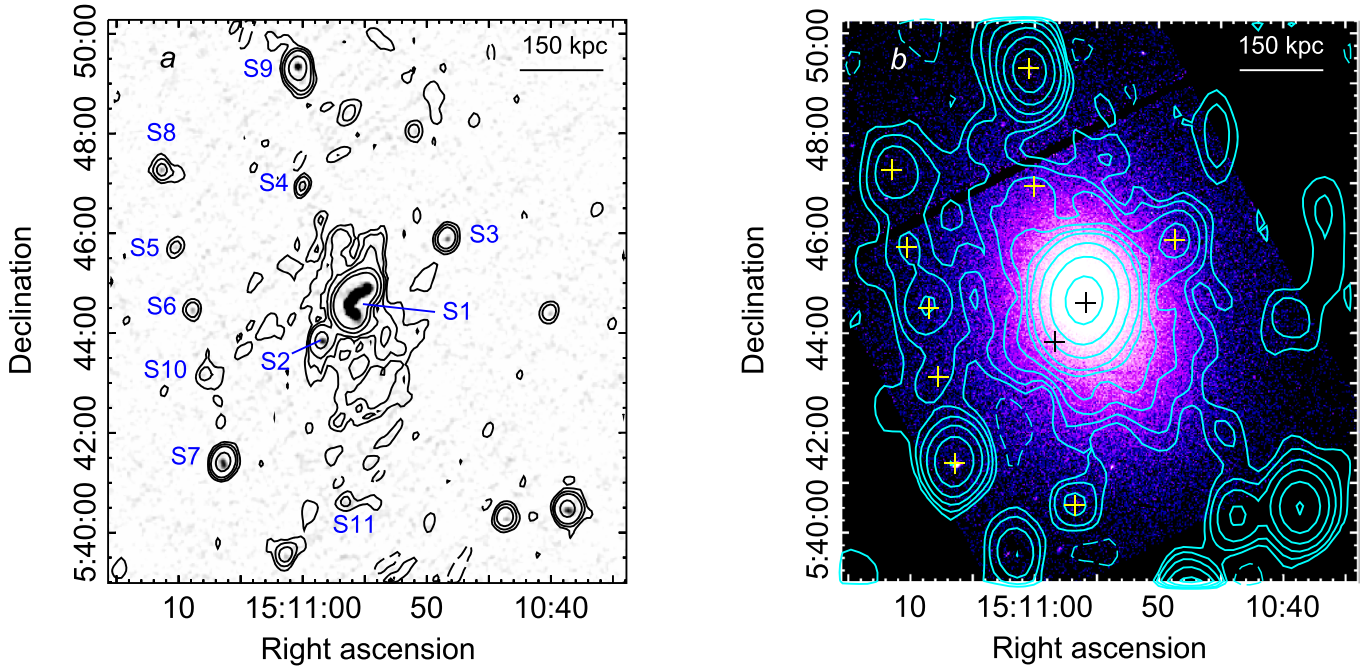

Figure 12. A2029. (a) VLA 1.4 GHz C-configuration contours, overlaid on the B-configuration image. The restoring beam and rms noise are $20'' \times 16''$ and $1\sigma = 30\mu$ Jy beam^{-1} and $5'' \times 4''$ and $1\sigma = 50$ μJy beam^{-1}, respectively. Contours are -0.1 (dashed), 0.1, 0.2, 0.4, 1.6, and 6.4 mJy beam^{-1}. The individual radio galaxies are labeled. (b) VLA 1.4 GHz D-configuration contours of the minihalo and radio galaxies (yellow and black crosses; see panel (a)), overlaid on the *Chandra* image in the 0.5–4 keV band. The radio image has a restoring beam of $57'' \times 45''$. The rms noise is $1\sigma = 40$ μJy beam^{-1}. Contours are -0.12 (dashed), 0.12, 0.24, 0.48, 0.96, 2, 4, 16, 64, and 256 mJy beam^{-1}.

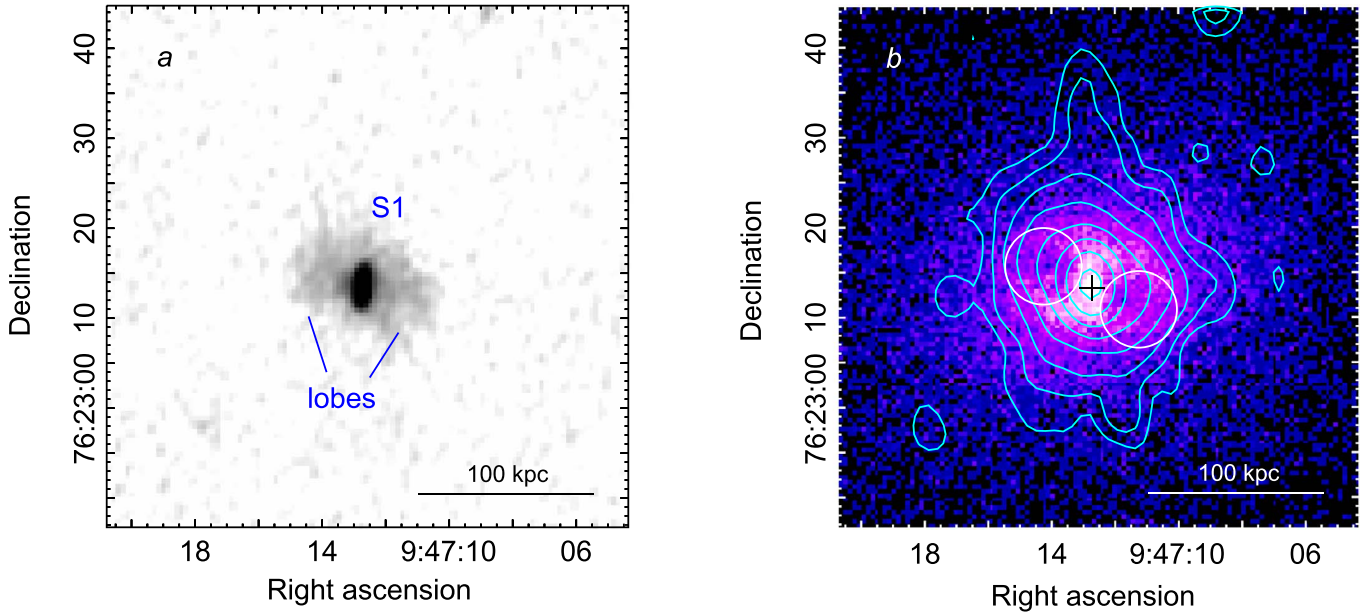

Figure 13. RBS 797. (a) VLA 1.4 GHz A-configuration image, restored with a $2'' \times 1''$ beam. The rms noise is $1\sigma = 17$ μJy beam^{-1}. The central radio galaxy S1 and the radio lobes filling the X-ray cavities (white circles in panel (b)) are labeled. (b) VLA 1.4 GHz B-configuration contours overlaid on the *Chandra* image in the 0.5–4 keV band. The radio image has a restoring beam of $5'' \times 4''$. The rms noise is $1\sigma = 27$ μJy beam^{-1}. Contours start at 70 μJy beam^{-1} and then scale by a factor of 2. No levels at -3σ are present in the portion of the image shown. Circles mark the X-ray cavities filled by the radio lobes (panel (a)).

Figure 11. We identified 10 discrete radio sources in the minihalo area (Table 9) using an image at $92'' \times 39''$ resolution, shown in panel (a). These sources account for a total flux of $S_{1.4\,\mathrm{GHz}} = 733.8$ mJy. To measure the minihalo flux density, we used a lower-resolution image, shown as contours in panel (b) on the *XMM-Newton* X-ray image. We subtracted the contribution from discrete sources. We also masked the region marked by a circle, which coincides with an X-ray cavity suggested by the *Chandra* and *XMM-Newton* images of the cluster core (Werner et al. 2016; S. Giacintucci et al. 2019, in preparation). The cavity is filled by a very steep spectrum relic lobe, likely inflated by a previous outburst of the central AGN

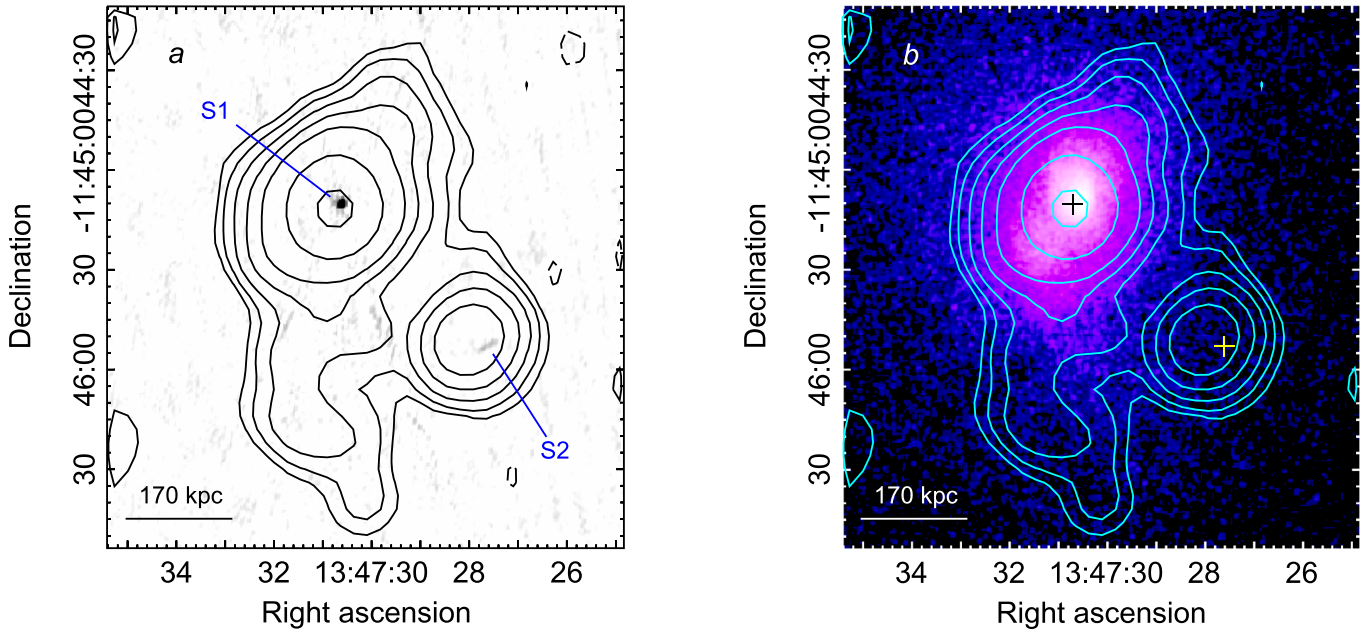

Figure 14. RX J1347.5–1145. (a) VLA 1.4 GHz C-configuration contours, overlaid on the 1.4 GHz A-configuration image. The restoring beam and rms noise are 17″ and $1\sigma = 40$ μJy beam^{-1} and 1.″2 and $1\sigma = 35$ μJy beam^{-1}, respectively. Contours are -0.12 (dashed), 0.12, 0.24, 0.48, 0.96, 2, 8, 32, and 128 mJy beam^{-1}. Individual radio galaxies are labeled. (b) VLA 1.4 GHz C-configuration contours of the minihalo and radio galaxies (black and yellow crosses; see panel (a)), overlaid on the *Chandra* image in the 0.5–4 keV band.

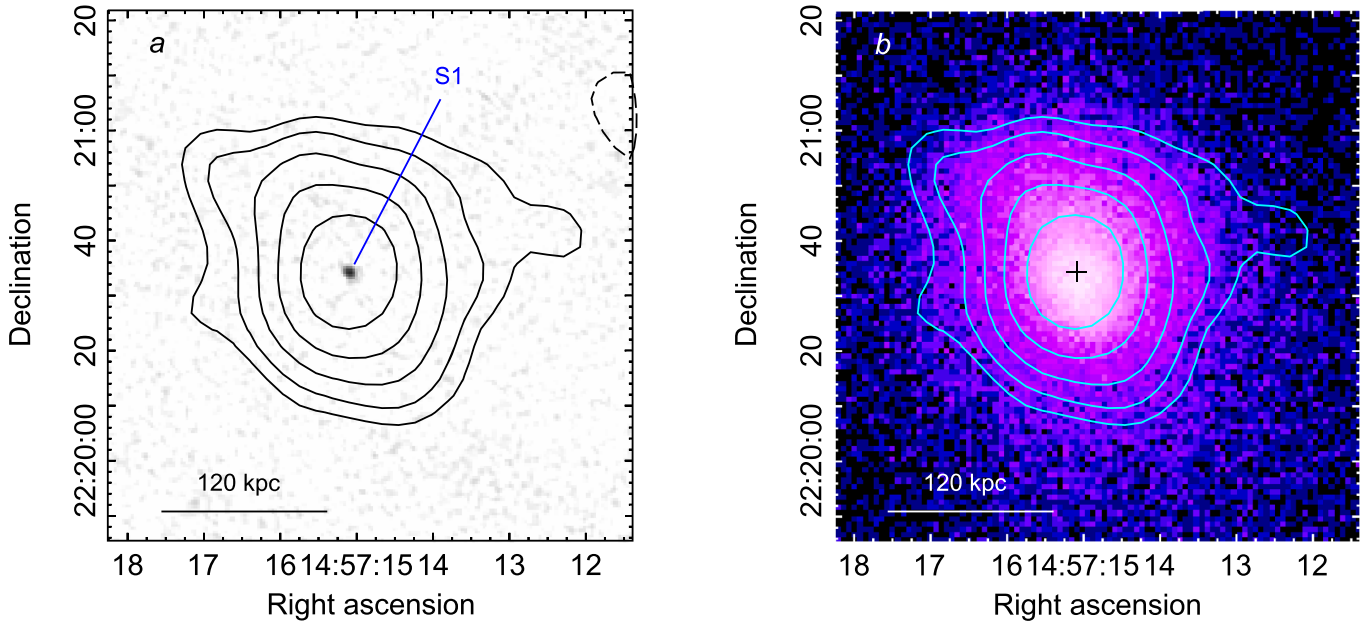

Figure 15. MS 1455.0+2232. (a) VLA 1.4 GHz C-configuration contours, overlaid on the 1.4 GHz A-configuration image. The restoring beam and rms noise are 16″ × 15″ and $1\sigma = 70$ μJy beam^{-1} and 1.″5 × 1.″2 and $1\sigma = 55$ μJy beam^{-1}, respectively. Contours are -1 (dashed), 1, 2, 4, 8, 16, ...×3σ, and S1 is the central radio galaxy. (b) VLA 1.4 GHz C-configuration contours of the minihalo and radio galaxy (black cross), overlaid on the *Chandra* image in the 0.5–4 keV band.

discovered in GMRT and *MWA* images at lower frequencies (S. Giacintucci et al. 2019, in preparation). The relic lobe is only partially visible at 1.4 GHz (Figure 11(b)). We obtained a total flux of $S_{\rm MH,1.4\,GHz} = 62 \pm 9$ mJy for the minihalo ($P_{\rm MH,1.4\,GHz} = (0.11 \pm 0.02) \times 10^{24}$ W Hz^{-1}). A higher flux of $106.4^{+10.4}_{-8.9}$ mJy has been measured by Govoni et al. (2009) using an exponential model to fit the surface brightness profile of the minihalo. A flux density of 85 ± 3 mJy is reported by the same authors by integration within a radius of ∼230 kpc. We note, however, that both of these measurements include part of the emission from the newly detected relic lobe. The flux density of the BCG is $S_{\rm BCG,1.4\,GHz} = 30.6 \pm 1.5$ mJy, and its radio power is $P_{\rm MH,1.4\,GHz} = (0.064 \pm 0.003) \times 10^{24}$ W Hz^{-1}.

A2029. A central minihalo was reported by Govoni et al. (2009). Our images are presented in Figure 12. We identified 11 discrete radio sources (Table 9), including the central dominant wide-angle tail (e.g., Taylor et al. 1994), using the B- and C-configuration images (panel (a)). The discrete sources

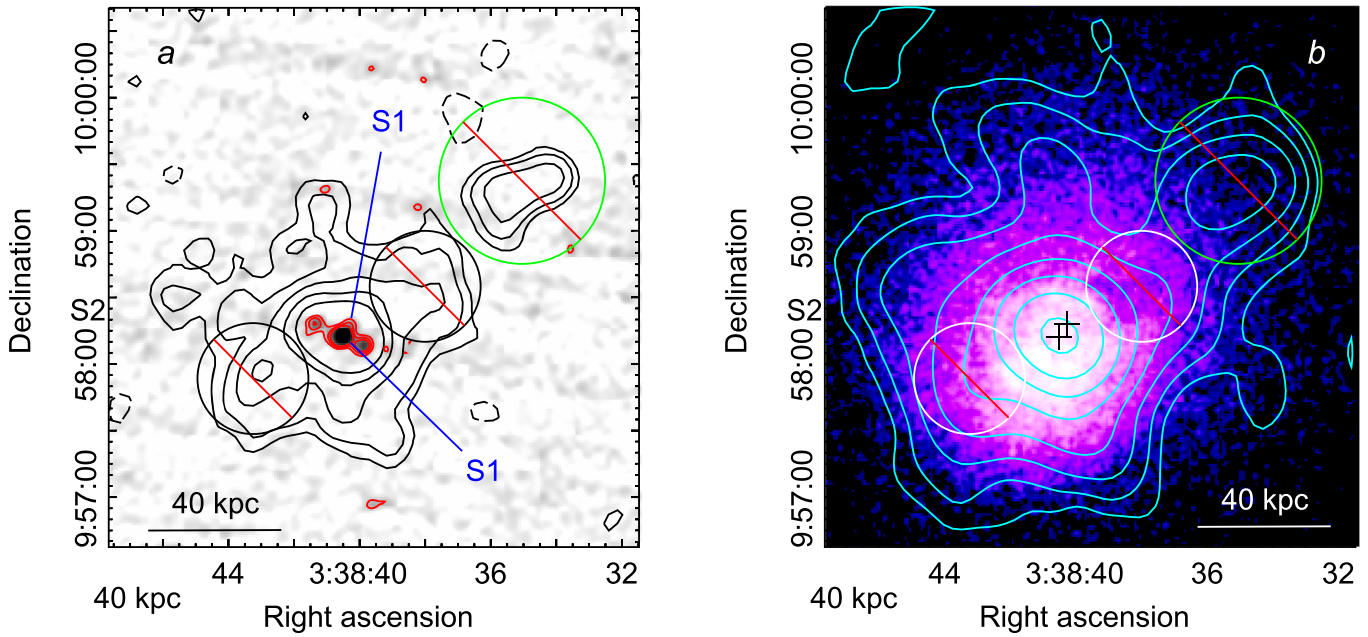

Figure 16. 2A 0335+096. (a) VLA 1.4 GHz C-configuration contours, overlaid on the 1.4 GHz B-configuration image (gray scale and red contours at $+3\sigma$, 6σ, and 10σ). The restoring beam and rms noise are $15'' \times 14''$ and $1\sigma = 35$ mJy beam^{-1} and $4''$ and $1\sigma = 58$ μJy beam^{-1}, respectively. Black contours are -1 (dashed), 1, 2, 4, 8, 16, ... $\times 3\sigma$. The central radio galaxy and nearby companion are labeled S1 and S2. Black circles mark the positions of two X-ray cavities filled by fossil radio lobes (S. Giacintucci et al. 2019, in preparation). The green circle marks the location of another possible fossil radio lobe. (b) VLA 1.4 GHz C+D-configuration contours of the minihalo and radio galaxies (black crosses; see panel (a)), overlaid on the *Chandra* image in the 0.5–4 keV band. The radio image has a restoring beam of $30'' \times 27''$. The rms noise is $1\sigma = 40$ μJy beam^{-1}. Contours are 1, 2, 4, 8, 16, . . . $\times 3\sigma$. No levels at -3σ are present in the portion of the image shown. The regions occupied by the X-ray cavities and fossil lobes (white and green circles) have been excluded to measure the flux density of the minihalo.

account for a total of $S_{1.4\ \mathrm{GHz}} = 531.2$ mJy. We used the D-configuration observation to map the minihalo (panel (b)) and measure its flux density. Our value of $S_{\mathrm{MH},1.4\ \mathrm{GHz}} = 19.5 \pm 2.5$ mJy, after removal of the flux in discrete sources, is in agreement within the errors with 18.8 ± 1.3 mJy measured by Govoni et al. (2009). The 1.4 GHz radio luminosity of the minihalo is $P_{\mathrm{MH},1.4\ \mathrm{GHz}} = (0.28 \pm 0.04) \times 10^{24}$ W Hz^{-1}. The flux density of the BCG is $S_{\mathrm{BCG},1.4\ \mathrm{GHz}} = 513 \pm 26$ mJy, and its radio power is $P_{\mathrm{BCG},1.4\ \mathrm{GHz}} = (7.4 \pm 0.4) \times 10^{24}$ W Hz^{-1}.

RBS 797. A central minihalo was reported by Gitti et al. (2006) and Doria et al. (2012). Our images are presented in Figure 13. Using the A-configuration image (panel (a)), we measure a radio flux density of $S_{\mathrm{BCG},1.4\ \mathrm{GHz}} = 17.9 \pm 0.9$ mJy ($P_{\mathrm{BCG},1.4\ \mathrm{GHz}} = (7.6 \pm 0.4) \times 10^{24}$ W Hz^{-1}) for the BCG (S1), which includes the central compact component and the two radio lobes associated with a pair of X-ray cavities (circles in panel (b); see Gitti et al. 2006; Doria et al. 2012). The flux density of the whole radio emission detected by the B-configuration image (b) is $S_{\mathrm{tot},1.4\ \mathrm{GHz}} = 23.1 \pm 1.1$ mJy, in agreement within the errors with the 24 ± 0.3 mJy reported by Doria et al. (2012). Once we have removed the BCG flux from the total emission, we find a residual flux of $S_{\mathrm{MH},1.4\ \mathrm{GHz}} = 5.2 \pm 0.6$ mJy for the minihalo (a flux density of 6.1 ± 0.4 mJy was estimated by Doria et al.), corresponding to $P_{\mathrm{MH},1.4\ \mathrm{GHz}} = (2.20 \pm 0.24) \times 10^{24}$ W Hz^{-1}.

RX J1347.5–1145. A central minihalo was reported by Gitti et al. (2007). Our images are presented in Figure 14. The central radio galaxy is a point source in the 1.4 GHz image from the A configuration (panel (a)). Its flux density is $S_{\mathrm{BCG},1.4\ \mathrm{GHz}} = 30.3 \pm 1.5$ mJy, and its luminosity is $P_{\mathrm{BCG},1.4\ \mathrm{GHz}} = (22.7 \pm 1.1) \times 10^{24}$ W Hz^{-1}. A much fainter and extended source (S2) is also detected, with a flux of $S_{\mathrm{S2},1.4\ \mathrm{GHz}} = 2.0 \pm 0.1$ mJy within the 3σ isocontour. Its flux density increases to 4.9 ± 0.2 mJy in the lower-resolution image from the C configuration, where the source becomes unresolved. This flux difference is likely due to missing extended emission in the A-configuration image. Similar flux density values for S1 and S2 were measured by Gitti et al. (2007) using the same radio data analyzed here. The total flux in the C-configuration image is $S_{\mathrm{tot},1.4\ \mathrm{GHz}} = 69.3 \pm 3.5$ mJy, measured out to a radius of $r = 80''$, where the integrated flux reaches saturation (Section 2.1). The total flux reported by Gitti et al. (2007) is ~25% lower than our measured flux. However, if we integrate the flux density within the 3σ isocontour of our C-configuration image, we obtain 60 ± 3 mJy, which is consistent within 1.5σ with Gitti et al. (2007). After removal of S1 and S2 from the total flux, we estimate $S_{\mathrm{MH},1.4\ \mathrm{GHz}} = 35.6 \pm 2.9$ mJy for the minihalo. The error includes the uncertainty in the subtraction of S2 using its flux from the A- or C-configuration images. The minihalo luminosity at 1.4 GHz is $P_{\mathrm{MH},1.4\ \mathrm{GHz}} = (26.7 \pm 2.1) \times 10^{24}$ W Hz^{-1}.

MS 1455.0+2232 (Z7160). The minihalo, first detected by Venturi et al. (2008) with the GMRT at 610 MHz, is only marginally extended in the VLA C-configuration image at 1.4 GHz (Figure 15). The central compact radio galaxy has $S_{\mathrm{BCG},1.4\ \mathrm{GHz}} = 4.7 \pm 0.2$ mJy in the A-configuration image, corresponding to $P_{\mathrm{BCG},1.4\ \mathrm{GHz}} = (0.96 \pm 0.05) \times 10^{24}$ W Hz^{-1}. The total integrated flux density in the C-configuration image is $S_{\mathrm{tot},1.4\ \mathrm{GHz}} = 13.2 \pm 0.7$ mJy, the minihalo accounting for $S_{\mathrm{MH},1.4\ \mathrm{GHz}} = 8.5 \pm 1.1$ mJy ($P_{\mathrm{MH},1.4\ \mathrm{GHz}} = (1.75 \pm 0.23) \times 10^{24}$ W Hz^{-1}). The BCG and minihalo flux densities at 610 MHz are $S_{\mathrm{BCG},610\ \mathrm{MHz}} = 9.5 \pm 0.8$ and $S_{\mathrm{MH},610\ \mathrm{MHz}} = 28.7 \pm 3.7$ mJy, respectively (Mazzotta & Giacintucci 2008).

Their spectral indices between 610 MHz and 1.4 GHz are $\alpha = 0.85 \pm 0.11$ and 1.46 ± 0.22.

2A 0335+096. A central minihalo was reported by Sarazin et al. (1995). Our 1.4 GHz images are presented in Figure 16. The central radio galaxy (S1) is a core-dominated, double-lobe source with a flux of $S_{\rm BCG,1.4\,GHz} = 16 \pm 1$ mJy in the B-configuration image (panel (a)). Its radio power is $P_{\rm BCG,1.4\,GHz} = (0.058 \pm 0.003) \times 10^{24}$ W Hz^{-1}. A nearby companion (S2) has $S_{\rm S2,1.4\,GHz} = 1.0 \pm 0.1$ mJy. Low-frequency GMRT images at 235 and 610 MHz reveal the presence of two fossil radio lobes associated with a previous outburst of the central AGN, opposite with respect to S1 and aligned along a northwest–southeast axis (a paper is in preparation; see talk by Giacintucci at the Snowcluster 2018 conference[15] for an image at 610 MHz). Their position is marked by white circles in Figure 16(b). The northwest lobe fills a prominent X-ray cavity seen in the *Chandra* image (Mazzotta et al. 2003; Sanders et al. 2009). A distinct patch of extended emission is detected at $\sim 25''$ ($\sim$18 kpc) from the cluster center (green circle). This feature becomes more prominent at lower frequencies due to its very steep radio spectrum and is interpreted as a fossil lobe from an even older AGN outburst. We measure a total flux of $S_{\rm tot,1.4\,GHz} = 48 \pm 2$ mJy in the combined C+D-configuration image (panel (b)). To estimate the 1.4 GHz flux density of the minihalo, we subtract the flux of S1 and S2 from the total emission, as well as the flux in the fossil lobes (southeast lobe: 4.1 ± 0.2 mJy; northwest lobe: 2.7 ± 0.1 mJy; outer northwest lobe: 3.1 ± 0.2 mJy). We obtain $S_{\rm MH,1.4\,GHz} = 21.1 \pm 2.1$ mJy and $P_{\rm MH,1.4\,GHz} = (0.06 \pm 0.01) \times 10^{24}$ W Hz^{-1}.

ORCID iDs

Simona Giacintucci https://orcid.org/0000-0002-1634-9886
Maxim Markevitch https://orcid.org/0000-0003-0144-4052
Rossella Cassano https://orcid.org/0000-0003-4046-0637
Tracy E. Clarke https://orcid.org/0000-0001-6812-7938

References

Aharonian, F. A., Akamatsu, H., Akimoto, F., et al. 2017, ApJL, 837, L15
Akritas, M. G., & Bershady, M. A. 1996, ApJ, 470, 706
Becker, R. H., White, R. L., & Helfand, D. J. 1995, ApJ, 450, 559
Böhringer, H., Schuecker, P., Guzzo, L., et al. 2004, A&A, 425, 367
Bravi, L., Gitti, M., & Brunetti, G. 2016, MNRAS, 455, L41
Briggs, D. S. 1995, BAAS, 27, 112.02
Brunetti, G., Giacintucci, S., Cassano, R., et al. 2008, Natur, 455, 944
Brunetti, G., & Jones, T. W. 2014, IJMPD, 23, 1430007
Burns, J. O., Sulkanen, M. E., Gisler, G. R., & Perley, R. A. 1992, ApJL, 388, L49
Cassano, R., Ettori, S., Brunetti, G., et al. 2013, ApJ, 777, 141
Cassano, R., Gitti, M., & Brunetti, G. 2008, A&A, 486, L31
Cavagnolo, K. W., Donahue, M., Voit, G. M., & Sun, M. 2009, ApJS, 182, 12, (C09)
Chambers, K. C., Magnier, E. A., Metcalfe, N., et al. 2016, arXiv:1612.05560
Chandra, P., Ray, A., & Bhatnagar, S. 2004, ApJ, 612, 974
Condon, J. J. 1992, ARA&A, 30, 575
Condon, J. J., Cotton, W. D., Greisen, E. W., et al. 1998, AJ, 115, 1693
Covone, G., Adami, C., Durret, F., et al. 2006, A&A, 460, 381
Crawford, C. S., Allen, S. W., Ebeling, H., Edge, A. C., & Fabian, A. C. 1999, MNRAS, 306, 857
David, L. P., Slyz, A., Jones, C., et al. 1993, ApJ, 412, 479
Doria, A., Gitti, M., Ettori, S., et al. 2012, ApJ, 753, 47
Fujita, Y., Kohri, K., Yamazaki, R., & Kino, M. 2007, ApJL, 663, L61
Fujita, Y., & Ohira, Y. 2013, MNRAS, 428, 599
Gendron-Marsolais, M., Hlavacek-Larrondo, J., van Weeren, R. J., et al. 2017, MNRAS, 469, 3872
Giacintucci, S., Markevitch, M., Brunetti, G., et al. 2014a, ApJ, 795, 73
Giacintucci, S., Markevitch, M., Brunetti, G., Cassano, R., & Venturi, T. 2011, A&A, 525, L10
Giacintucci, S., Markevitch, M., Cassano, R., et al. 2017, ApJ, 841, 71, (G17)
Giacintucci, S., Markevitch, M., Venturi, T., et al. 2014b, ApJ, 781, 9, (G14a)
Gitti, M., Brunetti, G., Cassano, R., & Ettori, S. 2018, A&A, 617, A11
Gitti, M., Brunetti, G., Feretti, L., & Setti, G. 2004, A&A, 417, 1
Gitti, M., Brunetti, G., & Setti, G. 2002, A&A, 386, 456
Gitti, M., Feretti, L., & Schindler, S. 2006, A&A, 448, 853
Gitti, M., Ferrari, C., Domainko, W., Feretti, L., & Schindler, S. 2007, A&A, 470, L25
Gitti, M., Tozzi, P., Brunetti, G., et al. 2015, in Advancing Astrophysics with the Square Kilometre Array (AASKA14), 76
Govoni, F., Murgia, M., Markevitch, M., et al. 2009, A&A, 499, 371
Guo, F., & Oh, S. P. 2008, MNRAS, 384, 251
Hitomi Collaboration, Aharonian, F., Akamatsu, H., et al. 2016, Natur, 535, 117
Hlavacek-Larrondo, J., Allen, S. W., Taylor, G. B., et al. 2013, ApJ, 777, 163
Hogan, M. T., Edge, A. C., Hlavacek-Larrondo, J., et al. 2015, MNRAS, 453, 1201
Ikebe, Y., Reiprich, T. H., Böhringer, H., Tanaka, Y., & Kitayama, T. 2002, A&A, 383, 773
Jacob, S., & Pfrommer, C. 2017, MNRAS, 467, 1478
Kalberla, P. M. W., Burton, W. B., Hartmann, D., et al. 2005, A&A, 440, 775
Kale, R., Venturi, T., Giacintucci, S., et al. 2013, A&A, 557, A99
Kale, R., Venturi, T., Giacintucci, S., et al. 2015, A&A, 579, A92, (K15)
Keshet, U., & Loeb, A. 2010, ApJ, 722, 737
Keshet, U., Markevitch, M., Birnboim, Y., & Loeb, A. 2010, ApJL, 719, L74
Macario, G., Venturi, T., Brunetti, G., et al. 2010, A&A, 517, A43
Markevitch, M., Mazzotta, P., Vikhlinin, A., et al. 2003, ApJL, 586, L19
Markevitch, M., Ponman, T. J., Nulsen, P. E. J., et al. 2000, ApJ, 541, 542
Markevitch, M., & Vikhlinin, A. 2007, PhR, 443, 1
Maughan, B. J., Giles, P. A., Randall, S. W., Jones, C., & Forman, W. R. 2012, MNRAS, 421, 1583
Mazzotta, P., Edge, A. C., & Markevitch, M. 2003, ApJ, 596, 190
Mazzotta, P., & Giacintucci, S. 2008, ApJL, 675, L9
McDonald, M., Allen, S. W., Bayliss, M., et al. 2017, ApJ, 843, 28
McDonald, M., McNamara, B. R., van Weeren, R. J., et al. 2015, ApJ, 811, 111
McNamara, B. R., & Nulsen, P. E. J. 2007, ARA&A, 45, 117
McNamara, B. R., & Nulsen, P. E. J. 2012, NJPh, 14, 055023
Murgia, M., Eckert, D., Govoni, F., et al. 2010, A&A, 514, A76
Perley, R. A., & Butler, B. J. 2013, ApJS, 204, 19
Pfrommer, C. 2013, ApJ, 779, 10
Pfrommer, C., & Enßlin, T. A. 2004, A&A, 413, 17
Piffaretti, R., Arnaud, M., Pratt, G. W., Pointecouteau, E., & Melin, J.-B. 2011, A&A, 534, A109
Planck Collaboration, Ade, P. A. R., Aghanim, N., et al. 2014, A&A, 571, 29
Ruszkowski, M., Yang, H.-Y. K., & Reynolds, C. S. 2017, ApJ, 844, 13
Sanders, J. S., Fabian, A. C., & Taylor, G. B. 2009, MNRAS, 396, 1449
Sarazin, C. L., Baum, S. A., & O'Dea, C. P. 1995, ApJ, 451, 125
Savini, F., Bonafede, A., Brüggen, M., et al. 2018, MNRAS, 478, 2234
Savini, F., Bonafede, A., Brüggen, M., et al. 2019, A&A, 622, A24
Sijbring, L. G. 1993, PhD thesis, Univ. Groningen
Storm, E., Jeltema, T. E., & Rudnick, L. 2015, MNRAS, 448, 2495
Taylor, G. B., Barton, E. J., & Ge, J. 1994, AJ, 107, 1942
van Haarlem, M. P., Wise, M. W., Gunst, A. W., et al. 2013, A&A, 556, A2
van Weeren, R. J., de Gasperin, F., Akamatsu, H., et al. 2019, SSRv, 215, 16
van Weeren, R. J., Intema, H. T., Lal, D. V., et al. 2014, ApJL, 786, L17
Venturi, T., Giacintucci, S., Brunetti, G., et al. 2007, A&A, 463, 937
Venturi, T., Giacintucci, S., Dallacasa, D., et al. 2008, A&A, 484, 327
Venturi, T., Rossetti, M., Brunetti, G., et al. 2017, A&A, 603, A125
Vikhlinin, A., Burenin, R. A., Ebeling, H., et al. 2009, ApJ, 692, 1033
Vikhlinin, A., Markevitch, M., Murray, S. S., et al. 2005, ApJ, 628, 655
Werner, N., Zhuravleva, I., Canning, R. E. A., et al. 2016, MNRAS, 460, 2752
Yang, H.-Y. K., & Reynolds, C. S. 2016, ApJ, 829, 90
Zandanel, F., Pfrommer, C., & Prada, F. 2014, MNRAS, 438, 124
Zhuravleva, I., Churazov, E., Schekochihin, A. A., et al. 2014, Natur, 515, 85
ZuHone, J. A., Brunetti, G., Giacintucci, S., & Markevitch, M. 2015, ApJ, 801, 146
ZuHone, J. A., Markevitch, M., Brunetti, G., & Giacintucci, S. 2013, ApJ, 762, 78
ZuHone, J. A., Markevitch, M., & Johnson, R. E. 2010, ApJ, 717, 908

[15] http://www.physics.utah.edu/snowcluster/archive/2018/talks/Giacintucci.pdf.